

## **INFORMATION TO USERS**

**This manuscript has been reproduced from the microfilm master. UMI films the text directly from the original or copy submitted. Thus, some thesis and dissertation copies are in typewriter face, while others may be from any type of computer printer.**

**The quality of this reproduction is dependent upon the quality of the copy submitted. Broken or indistinct print, colored or poor quality illustrations and photographs, print bleedthrough, substandard margins, and improper alignment can adversely affect reproduction.**

**In the unlikely event that the author did not send UMI a complete manuscript and there are missing pages, these will be noted. Also, if unauthorized copyright material had to be removed, a note will indicate the deletion.**

**Oversize materials (e.g., maps, drawings, charts) are reproduced by sectioning the original, beginning at the upper left-hand corner and continuing from left to right in equal sections with small overlaps.**

**ProQuest Information and Learning  
300 North Zeeb Road, Ann Arbor, MI 48106-1346 USA  
800-521-0600**

**UMI<sup>®</sup>**



**REGULARIZATION OF THE IMAGE DIVISION  
APPROACH TO BLIND DECONVOLUTION**

by  
Sergio Barraza-Felix

---

A Dissertation Submitted to the Faculty of the  
**COMMITTEE ON OPTICAL SCIENCES (GRADUATE)**  
In Partial Fulfillment of the Requirements  
For the Degree of  
**DOCTOR OF PHILOSOPHY**  
In the Graduate College  
**THE UNIVERSITY OF ARIZONA**

F a l l 2 0 0 2

UMI Number: 3073190

UMI<sup>®</sup>

---

UMI Microform 3073190

Copyright 2003 by ProQuest Information and Learning Company.  
All rights reserved. This microform edition is protected against  
unauthorized copying under Title 17, United States Code.

---

ProQuest Information and Learning Company  
300 North Zeeb Road  
P.O. Box 1346  
Ann Arbor, MI 48106-1346

THE UNIVERSITY OF ARIZONA ©  
GRADUATE COLLEGE

As members of the Final Examination Committee, we certify that we have read the dissertation prepared by Sergio Barraza-felix

entitled Regularization of the Image Division

Approach to Blind Deconvolution

\_\_\_\_\_  
\_\_\_\_\_  
\_\_\_\_\_

and recommend that it be accepted as fulfilling the dissertation requirement for the Degree of Doctor of Philosophy

B. Roy Frieden  
B. Roy Frieden

11/15/02  
Date

Hans Roehrig  
Hans Roehrig

11/15/02  
Date

William J. Dallas  
William J. Dallas

11/15/02  
Date

\_\_\_\_\_  
Date

\_\_\_\_\_  
Date

Final approval and acceptance of this dissertation is contingent upon the candidate's submission of the final copy of the dissertation to the Graduate College.

I hereby certify that I have read this dissertation prepared under my direction and recommend that it be accepted as fulfilling the dissertation requirement.

B. Roy Frieden  
Dissertation Director, B. Roy Frieden

11/15/02  
Date

## STATEMENT BY AUTHOR

This dissertation has been submitted in partial fulfillment of requirements for an advanced degree at The University of Arizona and is deposited in the University Library to be made available to borrowers under rules of the Library.

Brief quotations from this dissertation are allowable without special permission, provided that accurate acknowledgment of source is made. Requests for permission for extended quotation from or reproduction of this manuscript in whole or in part may be granted by the head of the major department or the Dean of the Graduate College when in his or her judgment the proposed use of the material is in the interests of scholarship. In all other instances, however, permission must be obtained from the author.

SIGNED: \_\_\_\_\_

A handwritten signature in cursive script, appearing to read "Sergio Benitez", is written over a horizontal line.

## ACKNOWLEDGMENTS

First I have to thank my family for giving me the necessary strength to complete this rough journey.

I owe a great debt to my advisor Dr. B. Roy Frieden. Thanks to his guidance and patience I could finish this work.

I especially must thank Dr. Shoemaker and the OSC staff, in particular Didi Lawson, who always help me without hesitation.

I also want to thank Candido Pinto. He was the one who helped me to overcome most of the computer related problems that I confronted during this work.

This research would not have been possible without the support of CONACYT (Mexico), and the University of Sonora (Mexico).

## DEDICATION

To the memory of my mother.

To my father.

To my three sons.

Sergio, Ernesto and Alejandro.

## TABLE OF CONTENTS

LIST OF FIGURES . . . . .	<b>8</b>
LIST OF TABLES . . . . .	<b>13</b>
ABSTRACT . . . . .	<b>14</b>
<b>CHAPTER 1. INTRODUCTION . . . . .</b>	<b>16</b>
1.1. Imaging Through a Turbulent Atmosphere . . . . .	16
1.2. Methods to Restore Images Degraded by Atmospheric Turbulence . . . . .	16
1.3. Regularization of the Image Division Method . . . . .	18
1.4. Outline of this Work . . . . .	19
<b>CHAPTER 2. THEORETICAL BACKGROUND . . . . .</b>	<b>21</b>
2.1. Fundamentals of Image Formation and Sampling . . . . .	21
2.1.1. Image Formation . . . . .	21
2.1.2. Fourier Transform . . . . .	22
2.1.3. Sampling . . . . .	23
2.2. Deconvolution . . . . .	24
2.2.1. Ordinary Deconvolution . . . . .	24
2.2.2. Linear Methods . . . . .	24
2.2.3. Non-Linear Methods . . . . .	26
2.3. Ill-Posed Problems and Regularization Approaches . . . . .	27
2.3.1. Ill-Posed Problems . . . . .	27
2.3.2. Ill-Conditioned System of Equations . . . . .	28
2.3.3. Regularization Approaches . . . . .	29
2.3.4. Least-Squares Solution . . . . .	30
2.4. Imaging Through a Turbulent Medium . . . . .	32
2.4.1. Atmospheric Turbulence . . . . .	32
2.4.2. Long- and Short-Exposure Pictures . . . . .	33
2.4.3. Computer Simulation of Atmospheric Turbulence . . . . .	35
<b>CHAPTER 3. REGULARIZATION OF THE IMAGE DIVISION METHOD . . . . .</b>	<b>37</b>
3.1. Image Division Method . . . . .	37
3.1.1. Image Turbulence Problem . . . . .	37
3.1.2. Overcoming the Homogeneity Problem . . . . .	40
3.2. Regularization of the Image Division Method . . . . .	42
3.2.1. Multiple Solutions . . . . .	42
3.2.2. Least-Squares Solution . . . . .	46

## LIST OF FIGURES

FIGURE 1.1. Simulated images of a star for a 1.5 m diameter telescope at 0.400 $\mu m$ wavelength. (a) Diffraction limited image for a perfect telescope with no atmospheric turbulence. The angular size for this image is about 0.02 arc seconds. (b) Short-exposure image of a star degraded by computer simulation of atmospheric turbulence. The coherence length, $r_o$ , is 30 cm.	17
FIGURE 2.1. Image formation of a point source through the atmosphere . . .	34
FIGURE 3.1. One-dimensional, eight pixels wide arbitrary object . . . . .	43
FIGURE 3.2. Two one-dimensional arbitrary PSF's. (a) $s^{(1)}$ . (b) $s^{(2)}$ . . . . .	43
FIGURE 3.3. Resulting two different images. (a) $i^{(1)}$ , (b) $i^{(2)}$ . . . . .	44
FIGURE 3.4. Reconstructed PSF 1 for different supports. (a) True $s^{(1)}$ , (b) reconstructed $s^{(1)}$ for 14 pixels support, (c) for 12 pixels supp., (d) for 10 pixels supp., (e) for 8 pixels supp., (f) for 6 pixels supp., (g) for 4 pixels supp., (h) for 2 pixels supp. . . . .	45
FIGURE 3.5. Flow chart for the image division program. . . . .	48
FIGURE 4.1. Two short-exposure images of a binary star system, for low turbulence $r_o = 0.2 m$ , no noise added case. (a) Image 1, (b) image 2. . . .	53
FIGURE 4.2. A binary star system. The stars are separated by 0.2 arc seconds (4 pixels). The dim star has a brightness which is about 40% of that of its neighbor sister (a) Original object. (b) Reconstruction for low turbulence $r_o = 0.2 m$ , no noise added case. . . . .	54
FIGURE 4.3. Two turbulent degraded PSF's, for the no added noise case. (a) PSF 1, (b) PSF 2, (c) Reconstructed PSF 1, (d) Reconstructed PSF 2. . .	55
FIGURE 4.4. Two short-exposure images of a binary star, for high turbulence, $r_o = 0.05 m$ , 1% additive Gaussian noise case. (a) Image 1, (b) Image 2.	56
FIGURE 4.5. Binary stars, high turbulence $r_o = 0.05 m$ , 1% additive Gaussian noise case. (a) Original object. (b) Reconstruction. . . . .	56
FIGURE 4.6. Two high-turbulent degraded PSF's, $r_o = 0.05 m$ , used for the 1% additive Gaussian noise case. (a) PSF 1. (b) PSF 2. (c) Reconstructed PSF 1. (d) Reconstructed PSF 2. . . . .	57
FIGURE 4.7. Two short-exposure images for high turbulence, $r_o = 0.05 m$ , 3% additive Gaussian noise case. (a) Image 1. (b) Image 2. . . . .	58
FIGURE 4.8. Binary star system, high turbulence, $r_o = 0.05 m$ , 3% additive Gaussian noise case. (a) Original object. (b) Reconstructed object. . . .	59
FIGURE 4.9. Two high turbulent degraded PSF's used for the 3% additive Gaussian noise case. (a) PSF 1. (b) PSF 2. (c) Reconstructed PSF 1. (d) Reconstructed PSF 2. . . . .	60

LIST OF FIGURES—*Continued*

FIGURE 4.10. Short-exposure pictures of binary stars for a low level of turbulence, $r_o = 0.2 m$ , and 5% additive Gaussian noise. (a) Image 1. (b) Image 2. . . . .	61
FIGURE 4.11. Binary stars. (a) Original object. (b) Reconstruction for a low level of turbulence, $r_o = 0.2 m$ , and 5% additive Gaussian noise. . . . .	61
FIGURE 4.12. Low turbulent degraded PSF's, for a 5% additive Gaussian noise case. (a) PSF 1. (b) PSF 2. (c) Reconstructed PSF 1. (d) Reconstructed PSF 2. . . . .	62
FIGURE 4.13. Two short-exposure images for a high level of turbulence, $r_o = 0.05 m$ , and 8% additive Gaussian noise. (a) Image 1. (b) Image 2. . . .	63
FIGURE 4.14. Binary stars. (a) Original object. (b) Reconstruction for high turbulence $r_o = 0.05 m$ , 8% additive Gaussian noise case. . . . .	63
FIGURE 4.15. Two high turbulent degraded PSF's used for the 8% additive Gaussian noise case. (a) PSF 1. (b) PSF 2. (c) Reconstructed PSF 1. (d) Reconstructed PSF 2. . . . .	64
FIGURE 4.16. Two short-exposure images of binary stars, for a low level of turbulence, $r_o = 0.2 m$ , and 10% of additive Gaussian noise. (a) Image 1. (b) Image 2. . . . .	65
FIGURE 4.17. Binary stars. (a) Original object. (b) Reconstruction for a low level of turbulence, $r_o = 0.2 m$ , and 10% additive Gaussian noise case. . . . .	65
FIGURE 4.18. Low turbulent degraded PSF's, for the 10% additive Gaussian noise case. (a) PSF 1. (b) PSF 2. (c) Reconstructed PSF 1. (d) Reconstructed PSF 2. . . . .	66
FIGURE 4.19. Two moderate turbulent degraded ( $r_o = 0.1 m$ ) images of the cluster of stars. They are corrupted with 3% additive Gaussian noise. (a) Image 1. (b) Image 2. . . . .	67
FIGURE 4.20. A cluster of stars. (a) Original object. (b) Reconstructed object for low level of turbulence, 0% additive Gaussian noise. (c) Reconstructed object for low level of turbulence, $r_o = 0.2 m$ , 1% additive Gaussian noise. (d) Reconstructed object for moderate level of turbulence, $r_o = 0.1 m$ , 3% additive Gaussian noise. (e) Reconstructed object for low level of turbulence, $r_o = 0.2 m$ , 5% additive Gaussian noise. (f) Reconstructed object for moderate level of turbulence, $r_o = 0.1 m$ , 8% additive Gaussian noise. . . . .	69
FIGURE 4.21. Two short-exposure pictures of a galaxy, for low turbulence $r_o = 0.2 m$ , 5% additive Gaussian noise case. (a) Image 1. (b) Image 2. . . . .	70

LIST OF FIGURES—*Continued*

FIGURE 4.22. A galaxy. (a) Original object. (b) Reconstruction for a low level of turbulence, $r_o = 0.2 m$ , and 0% additive Gaussian noise. (c) Reconstruction for a low level of turbulence, $r_o = 0.2 m$ , and 1% additive Gaussian noise. (d) Reconstruction for a low level of turbulence, $r_o = 0.2 m$ , and 3% additive Gaussian noise. (e) Reconstruction for a low level of turbulence, $r_o = 0.2 m$ , and 5% additive Gaussian noise. (f) Reconstruction for a low level of turbulence, $r_o = 0.2 m$ , and 8% additive Gaussian noise. . . . .	71
FIGURE 4.23. Two short-exposure images of a hot source. (a) Image 1. (b) Image 2. . . . .	72
FIGURE 4.24. Reconstructed object for the one hot source case. . . . .	73
FIGURE 4.25. Two short-exposure images of a two hot source target. (a) Image 1. (b) Image 2. . . . .	74
FIGURE 4.26. Reconstructed object for the two hot source target. . . . .	75
FIGURE 4.27. Two short-exposure images of a target composed by three hot sources. . . . .	76
FIGURE 4.28. Reconstructed object for the three hot source object. . . . .	77
FIGURE 4.29. The object (a), and the PSF (b) used by Ayers and Dainty, Lane and Holmes. . . . .	78
FIGURE 4.30. Second PSF used on the regularized image division method. . . . .	78
FIGURE 4.31. Reconstructed object for the noiseless case applying Ayers and Dainty's method. . . . .	79
FIGURE 4.32. Reconstructed PSF for the noiseless case applying Ayers and Dainty's method. . . . .	79
FIGURE 4.33. Results from the image division approach to the noiseless case. (a) Reconstructed object. (b) Reconstructed PSF. . . . .	80
FIGURE 4.34. Reconstructed object (a), and PSF (b), using Lane's method for a noiseless image. . . . .	80
FIGURE 4.35. Reconstructed object (a), and PSF (b), using Lane's method for an image corrupted with Poisson noise with $10^4$ photons as a mean number of photons at the brightest pixel in the convolution . . . . .	81
FIGURE 4.36. Reconstructed object (a), and PSF (b), using Lane's method for an image corrupted with Poisson noise with $10^3$ photons as a mean number of photons at the brightest pixel in the convolution . . . . .	81
FIGURE 4.37. Reconstructed object (a), and PSF (b), using Lane's method for an image corrupted with Poisson noise with $10^2$ photons as a mean number of photons at the brightest pixel in the convolution . . . . .	81

LIST OF FIGURES—*Continued*

FIGURE 4.38. Reconstructed object (a), and PSF 1 (b), using the image division algorithm for an image corrupted with Poisson noise with $10^4$ photons as a mean number of photons at the brightest pixel in the convolution . . .	82
FIGURE 4.39. Reconstructed object (a), and PSF 1 (b), using the image division algorithm for an image corrupted with Poisson noise with $10^3$ photons as a mean number of photons at the brightest pixel in the convolution. . .	82
FIGURE 4.40. Reconstructed object (a), and PSF 1 (b), using the image division algorithm for an image corrupted with Poisson noise with $10^2$ photons as a mean number of photons at the brightest pixel in the convolution . . .	83
FIGURE 4.41. Result from Holmes' method for a Poisson noise corrupted image with 4000 photons per pixel. . . . .	84
FIGURE 4.42. Result from Holmes' method for a Poisson noise corrupted image with 100 photons per pixel. . . . .	84
FIGURE 4.43. Result from the image division method for a Poisson noise corrupted images with 4000 photons per pixel. . . . .	85
FIGURE 4.44. Result from the image division method for a Poisson noise corrupted images with 100 photons per pixel. . . . .	86
FIGURE 5.1. Two random PSF's with different supports. (a) PSF with a $26 \times 26$ pixels support. (b) PSF with a $10 \times 10$ pixels support. . . . .	88
FIGURE 5.2. Two images formed with PSF's with different supports. (a) Image with a PSF $26 \times 26$ pixels. (b) Image with a PSF $10 \times 10$ pixels. . .	89
FIGURE 5.3. Reconstructed PSF's using the original images. . . . .	89
FIGURE 5.4. Reconstructed PSF's using the combined images. . . . .	90
FIGURE 5.5. Reconstructed objects. (a) Using the original images. (b) Using the combined images. . . . .	90
FIGURE 5.6. Plot of data inconsistency $e$ versus support component $\hat{K}_1$ for various values of component $\hat{K}_2$ : $\hat{K}_2 = \hat{K}_1 - 2$ (pluses, +), $\hat{K}_2 = \hat{K}_1 - 1$ (open circles, o), $\hat{K}_2 = \hat{K}_1$ (asterisks, *), $\hat{K}_2 = \hat{K}_1 + 1$ (crosses, x), $\hat{K}_2 = \hat{K}_1 + 2$ (continuous line). . . . .	92
FIGURE 5.7. Plot of polynomial fitting of data inconsistency $e$ versus support component $\hat{K}_1$ for various values of component $\hat{K}_2$ : $\hat{K}_2 = \hat{K}_1 - 2$ (dot line), $\hat{K}_2 = \hat{K}_1 - 1$ (continuous line), $\hat{K}_2 = \hat{K}_1$ (dashed line), $\hat{K}_2 = \hat{K}_1 + 1$ (dashed-dot line), $\hat{K}_2 = \hat{K}_1 + 2$ (continuous line). The cross points to the grand minimum at $\hat{K}_1 = 27$ and $\hat{K}_2 = 26$ pixels. . . . .	93
FIGURE 5.8. Reconstructions for the binary star system, low level of turbulence, 5% additive Gaussian noise case. (a) Reconstructed object for a support of $\hat{K}_1 = 27$ and $\hat{K}_2 = 26$ pixels. (b) Reconstructed object for a support of $\hat{K}_1 = 27$ and $\hat{K}_2 = 28$ pixels. . . . .	94

LIST OF FIGURES—*Continued*

FIGURE 5.9. The residual error for eqs. (3.19) and (3.20) for different levels of noise. (a) 1% (open circles), (b) 5% (pluses), (c) 10% (crosses), (d) Right-hand sides of eqs. (3.19) and (3.20) (asterisks) . . . . .	95
FIGURE 5.10. Singular values of matrix $H$ from eq. (3.21), for three levels of noise: (a) 0% (asterisks), (b) 5% (open circles), and (c) 10% (pluses). . .	96
FIGURE 5.11. Graphic of the relative error on $D_n$ : $\delta_n$ (pluses), and the absolute value of the image spectrum $I_n^{(2)}$ (open circles) versus frequency. . . . .	98

## LIST OF TABLES

TABLE 5.1. Values of $k$ for different levels of noise. . . . .	94
---	----

## ABSTRACT

Randomly inhomogeneous media, such as a turbulent atmosphere, degrade images taken by optical systems. This imposes strong limitations on the resolution achieved by optical systems. The quest for increasing the angular resolution of terrestrial telescopes is still open. This work is a small contribution in that quest.

A problem of blind deconvolution arises when one attempts to restore a short-exposure image that has been degraded by random atmospheric turbulence. The image division method attacks this problem by using two short-exposure images of the same object and taking the ratio of their respective Fourier transforms. The result is the quotient of the unknowns transfer functions. The latter are expressed as Fourier series in corresponding point-spread functions. Cross multiplying the division equation gives a system of linear equations with the point-spread functions as unknowns.

It is found that the system of linear equations, resulting from the implementation of the image division method, has a multiplicity of solutions. Moreover such system of equations is poorly conditioned. This brings the necessity of a regularization approach.

This dissertation describes the development and implementation of a regularization algorithm for the image division method. Using this regularization algorithm the blind deconvolution problem is posed as a constrained least-squares problem. A least-squares solution is found by computing a QR factorization of the system matrix. The Householder transformation method is used to find this factorization. The QR decomposition transforms the problem into an upper-triangular system of equations which is solved by backsubstitution. Prior partial knowledge about the point-spread functions and the object (such as finite support and positivity) is used to impose constraints on the solution, solving the multiplicity-solutions problem.

The regularization algorithm is tested with simulated and real data. Good quality reconstructions are obtained from the implementation of the regularized image division method on computer simulated atmospheric degraded images corrupted with up to 5% of additive Gaussian noise, or corrupted with Poisson noise with 100 or more photons as the average number of photons per pixel. It also yields good results when tested with real infrared short-exposure images.

## Chapter 1

# INTRODUCTION

## 1.1 Imaging Through a Turbulent Atmosphere

Imaging through a randomly inhomogeneous media imposes strong limitations on the resolution achieved by an optical system. Such is the case for terrestrial telescopes, where atmospheric turbulence limits the resolution of long-exposure pictures to approximately one arcsecond [1].

Variations in the air temperature, caused by the non-uniform heating of the sun and turbulent wind flow, produce inhomogeneities in the refractive index of the atmospheric air. The phase of light waves coming from celestial objects is disturbed, as the light passes through these inhomogeneities. This degrades the images formed by terrestrial telescopes. A typical short-exposure image of a star has a speckle-like structure [1]. Figure 1.1 shows a simulated diffraction limited image of a star (a), and a simulated turbulent degraded image of the same star (b). Note how the resolution is dramatically affected by atmospheric turbulence.

Increasing the angular resolution of terrestrial telescopes is still an open problem which demands the effort of many scientists and engineers working in different fields. This dissertation is a small step on that direction.

## 1.2 Methods to Restore Images Degraded by Atmospheric Turbulence

Several techniques have been proposed and used to restore images degraded by atmospheric turbulence. Correlation-based techniques such as Labeyrie's method [2] and triple correlation [3], [4] use a set of short exposure pictures to recover information



FIGURE 1.1. Simulated images of a star for a 1.5 m diameter telescope at  $0.400 \mu\text{m}$  wavelength. (a) Diffraction limited image for a perfect telescope with no atmospheric turbulence. The angular size for this image is about  $0.02 \text{ arc seconds}$ . (b) Short-exposure image of a star degraded by computer simulation of atmospheric turbulence. The coherence length,  $r_o$ , is 30 cm.

about the object up to the diffraction limit. However these methods do not directly obtain the object's intensity but, rather, the object's intensity autocorrelation. Consequently a phase-retrieval problem has to be solved to get an estimate of the object. Another disadvantage of these methods is that they usually require a reference point source to correct for atmospheric turbulence. In the case of such a point source, theoretical assumptions can often be made, but these are only approximately valid.

A second kind of technique uses wave-front sensors to measure the turbulent phase perturbation profile across each short exposure picture. Among them are self-referenced speckle holography [5], [6], which requires post-processing techniques to obtain an estimate of the object, and adaptive optics [7], [8], which uses deformable mirrors to correct the phase perturbation in real time. These techniques also require a nearby point source that is referred to as a guide star. It may be a star near the field of view or may be formed by projecting a focused laser beam into the atmosphere.

However since the light coming from the guide star does not pass through the same turbulence as the light coming from the object being imaged, it is possible that residual phase errors remain after the correction. Therefore post-processing techniques are sometimes used in adaptive optics. Furthermore the cost of the hardware needed for these techniques can be high, making them not available for some observing facilities.

A third kind of technique produces an estimate of the object's intensity from one or more short exposure pictures, without the use of a reference point source. Because both the object and PSF are unknown the problem is called "blind deconvolution". Examples of such approaches are the method developed by Ayers and Dainty [9], which alternately constrains the estimates of the object and PSF in the image and Fourier domains, and Lane's method [10], which reformulates the problem as an unconstrained minimization problem incorporating the image and Fourier constraints into an error metric. These are generally open-ended iterative searches, growing out of either a gradient search of solution space or a replacement algorithm (successive Fourier transformations and replacement).

### **1.3 Regularization of the Image Division Method**

The image division method was first proposed by Frieden in 1998 [11], as a means of attacking the problem of blind deconvolution in an efficient manner. It consists of using two short-exposure images of the same object and taking the ratio of their respective Fourier transforms. Because the object is the same, the ratio eliminates the object itself as a variable in the problem (ignoring added noise of detection), leaving behind the ratio of the spectra of the PSF's, from both exposures. This ratio is then transformed into a system of linear equations with the PSF's as unknowns. An ill-posed problem arises from the implementation of this method, since the system of equations has multiple solutions. Moreover such a system of equations is ill-conditioned. A regularization approach is needed in order to make the image

division method a useful tool in solving the blind deconvolution problem.

I have developed a regularization algorithm for this method. It consists of solving the mentioned system of equations by a least-squares approach, and using prior knowledge of the object and PSF's to impose constraints on the "acceptable" solution. The regularization approach works well in simulated noisy data (up to 5% of additive Gaussian noise), and in real images used to test it.

## 1.4 Outline of this Work

This dissertation describes my work at the Optical Sciences Center in the quest to regularize the image division approach to blind deconvolution. Regularizing the ill-posed problem that arises from the image division method is a complex task; it requires the overcoming of a non-unique solution scenario, and an ill-conditioned system of equations.

I have made a summary of the required concepts and equations in order to attack the problem of regularization of the image division method in Chapter 2. Also found there are the fundamentals of image formation and sampling, a brief description of some linear and non-linear deconvolution methods, the concept of ill-posed problem and regularization approaches, and some statistical properties used to describe the effect of atmospheric turbulence on imaging systems.

In Chapter 3 the image division method is described. It uses two short-exposure images to build up a linear system of equations with the elements of the PSF's of both images as the unknowns. Then the ill-posed problem arising from the application of this method is analyzed. It is found that the problem has multiple solutions, and that the system of equations resulting from this method is poorly conditioned. Finally a regularization algorithm for the image division method is presented. It is a fixed-length restoration approach that finds a least-squares solution to the problem, subject to positivity and finite support of the object and PSF's.

The regularization approach is tested with simulated and real data in Chapter 4. Simulated turbulent degraded images from different objects (a binary star system, a cluster of stars and a galaxy), with different degrees of turbulence (low, moderate and high) and levels of noise (0%, 1%, 3%, 5%, 8% and 10% additive Gaussian noise), are processed with the regularization algorithm, and the results are presented as images of the reconstructed objects and PSF's. Real images are also used. These are infrared images of hot sources taken at Kitt Peak by John Garcia. After processing, resulting images prove the effectiveness of the method when used with real data. In the last part of Chapter 4, results from the regularized image division method are compared to results from Ayers and Dainty's method [9], Lane's method [10] and Holmes' method [12].

Finally, in Chapter 5 several subjects are discussed. Among them are: a trick to cope with PSF's with different supports, a brief analysis of how data errors affect the system of equations, and a procedure to pose the blind deconvolution problem as a weighted least-squares problem. Conclusions of this work are also given in Chapter 5. There the partial achievement of the regularization of the image division method is noted. The advantages of the approach are described and some suggestions to improve it are proposed.

## Chapter 2

# THEORETICAL BACKGROUND

## 2.1 Fundamentals of Image Formation and Sampling

### 2.1.1 Image Formation

A great variety of optical imaging systems can be modeled as linear systems. That is, the system output  $g_{out}(\vec{x})$  can be expressed as a linear integral equation of the input  $g_{in}(\vec{x})$

$$g_{out}(\vec{x}) = \int_{-\infty}^{\infty} \int_{-\infty}^{\infty} d^2\vec{x}' g_{in}(\vec{x}') h(\vec{x}; \vec{x}'), \quad (2.1)$$

where  $h(\vec{x}; \vec{x}')$  is the point spread function (PSF), nominally, the impulse response of the system in question.

For incoherent illumination [13] an optical system produces an irradiance distribution  $i(\vec{x})$  at an image plane, from a spatial radiance exitance distribution  $o(\vec{x}')$  of the object being imaged. The connection between them, follows from (2.1) [15]

$$i(\vec{x}) = \int_{-\infty}^{\infty} \int_{-\infty}^{\infty} d^2\vec{x}' o(\vec{x}') s(\vec{x}; \vec{x}') + n(\vec{x}). \quad (2.2)$$

Again  $s(\vec{x}; \vec{x}')$  designates the PSF of the system. An additional term has been added to the right hand side of (2.2), to account for the multiple sources of noise present in the formation and detection of any image.

Aside from linearity some optical system exhibit another property called shift invariance or isoplanatism. For these systems the PSF depends only on  $\vec{x} - \vec{x}'$ , and eq. (2.2) takes the form

$$i(\vec{x}) = \int_{-\infty}^{\infty} \int_{-\infty}^{\infty} d^2\vec{x}' o(\vec{x}') s(\vec{x} - \vec{x}') + n(\vec{x}), \quad (2.3)$$

or

$$i(\vec{x}) = o(\vec{x}) \odot s(\vec{x}) + n(\vec{x}), \quad (2.4)$$

where the symbol  $\odot$  represents the convolution operation.

### 2.1.2 Fourier Transform

The importance of Fourier analysis in optics is well known. The two-dimensional Fourier transform (F.T.)  $G(\vec{k})$ <sup>1</sup> of a function  $g(\vec{x})$  is defined by [13]

$$G(\vec{k}) = \int_{-\infty}^{\infty} \int_{-\infty}^{\infty} d^2\vec{x} g(\vec{x}) \exp(-j\vec{k} \cdot \vec{x}), \quad (2.5)$$

where  $\vec{k}$  is an angular spatial frequency vector, in which its components  $k_1$  and  $k_2$  are given in units of radians/length.

Similarly the inverse Fourier transform (I.F.T.) is defined by [13]

$$g(\vec{x}) = \frac{1}{(2\pi)^2} \int_{-\infty}^{\infty} \int_{-\infty}^{\infty} d^2\vec{k} G(\vec{k}) \exp(j\vec{k} \cdot \vec{x}). \quad (2.6)$$

One of the most important properties of the Fourier transform is the denominated convolution theorem, which states that the F.T. of the convolution of two functions is equal to the product of their Fourier transforms [13]. Using this property, the eq. (2.4) in the Fourier domain becomes

$$I(\vec{k}) = \tau(\vec{k})O(\vec{k}) + N(\vec{k}), \quad (2.7)$$

where  $\tau(\vec{k})$  is known as the transfer function of the optical system. The advantage of working in the Fourier domain is apparent from the simplicity of (2.7)

A related concept, and a useful computational tool, is the discrete Fourier transform (DFT), which is defined by:

---

<sup>1</sup>In general the F.T. of a function  $f$  will be represented by the respective upper-case counterpart  $F$ . An exception is a PSF, whose F.T. is represented by the Greek letter  $\tau$ .

$$G_{n_1 n_2} = (\Delta x)^2 \sum_{m_1=0}^{N-1} \sum_{m_2=0}^{N-1} g_{m_1 m_2} \exp(-2\pi j(m_1 n_1 + m_2 n_2)/N^2) \quad (2.8)$$

### 2.1.3 Sampling

Frequently in optics, especially for data processing purposes, the image irradiance is sampled on a discrete set of points (actually small areas) using an electronic detector such as a charge-coupled device (CCD). That makes the image a discrete array of numbers  $i_{mn} = i(m\Delta x_1, n\Delta x_2)$  instead of a continuous function ( $\Delta x_1$  and  $\Delta x_2$  are the sampling intervals in  $x_1$  and  $x_2$  directions respectively). However a sampled version  $i_s(\vec{x})$  of the function  $i(\vec{x})$  can be constructed from this discrete array and the use of delta functions.

$$i_s(\vec{x}) = \sum_{n=-\infty}^{\infty} \sum_{m=-\infty}^{\infty} i_{mn} \delta(x_1 - m\Delta x_1) \delta(x_2 - n\Delta x_2). \quad (2.9)$$

It is intuitive that if the samples are taken finally the original function can be reconstructed with good accuracy by interpolation. However for some kind of functions the reconstruction can be exact. This result is the Whittaker-Shannon sampling theorem [13]. It states that a band limited function (its F.T. is nonzero over a finite region of the frequency space) can be recovered exactly from its sampled version, provided that the interval between samples is not greater than a certain limit. This limit is proportional to the reciprocal of the cut-off spatial frequency [ $\vec{k}_c = (k_{1c}, k_{2c})$ ] and is called the Nyquist interval

$$\Delta x_{1max} = \frac{\pi}{k_{1c}} \quad ; \quad \Delta x_{2max} = \frac{\pi}{k_{2c}}. \quad (2.10)$$

This result is easy to understand if the F.T. of  $i_s(\vec{x})$  is computed:

$$I_s(\vec{k}) = \sum_{n=-\infty}^{\infty} \sum_{m=-\infty}^{\infty} I(k_1 - 2\pi m/\Delta x_1, k_2 - 2\pi n/\Delta x_2). \quad (2.11)$$

It can be observed that such F.T. consists of infinite number of replicas of the original F.T.  $I(\vec{k})$ , each separated by a distance  $2\pi/\Delta x_1$  in the  $k_1$  direction and  $2\pi/\Delta x_2$  in the

$k_2$  direction. If the sampling interval is equal to or smaller than the Nyquist interval, then there is no overlap among these replica. Therefore the original spectrum can be recovered (and hence the original function) by an appropriate truncation of the series on (2.11).

## 2.2 Deconvolution

### 2.2.1 Ordinary Deconvolution

It is a common goal of image processing to find an estimate  $\hat{o}(\vec{x})$  of an unknown object  $o(\vec{x})$ , using the available data  $i(\vec{x})$ . The procedure to accomplish this goal is called "deconvolution". Often the PSF of the optical system is known. This is the case for ordinary deconvolution, which is the subject of this section<sup>2</sup>.

In general, deconvolution methods can be divided in linear and non-linear. Linear methods search for an estimate  $\hat{o}(\vec{x})$  through a series of linear operations over the data  $i(\vec{x})$ . In contrast, non-linear methods use prior knowledge of the unknown object to perform some kind of non-linear operations over the data to find an estimate of the object in question.

### 2.2.2 Linear Methods

Among these are the filtering methods, whose main advantage is computational speed. Filtering methods consist of multiplication of the image spectrum by a chosen filter function  $Y(\vec{k})$ ,

$$\hat{O}(\vec{k}) = Y(\vec{k})I(\vec{k}). \quad (2.12)$$

This is followed by an I.F.T. of  $\hat{O}(\vec{k})$  to yield an estimate  $\hat{o}(\vec{x})$

$$\hat{o}(\vec{x}) = \frac{1}{(2\pi)^2} \int_{-\infty}^{\infty} \int_{-\infty}^{\infty} d^2\vec{k} \hat{O}(\vec{k}) \exp(j\vec{k} \cdot \vec{x}). \quad (2.13)$$

---

<sup>2</sup>A good reference for ordinary deconvolution methods is Jansson [14].

If  $Y(\vec{k}) = \tau(\vec{k})$  the method is called inverse filtering. The major disadvantage of this method becomes evident in the realm of high spatial frequencies, where poor signal to noise ratio is a known issue. In such cases, noise amplification can lead to noisy estimate objects.

Another class of linear method results from the discrete version of (2.4) [14], [15]

$$i_n = \sum_m S_{n-m} o_m + n_n, \quad (2.14)$$

or in matrix notation

$$\vec{i} = \sum_m S \vec{o} + \vec{n}, \quad (2.15)$$

where  $\vec{i}$  and  $\vec{o}$  are column vectors with elements  $[\vec{i}]_n = i_n$  and  $[\vec{o}]_n = o_n$  respectively, and  $S$  is a matrix with elements given by  $[S]_{nm} = S_{n-m}$ .

There are several iterative methods to solve (2.15). Among them is Van Cittert's method, where the  $(p+1)^{th}$  approximation to the object is found from the  $p^{th}$  approximation through the expression

$$\hat{\vec{o}}^{(p+1)} = \hat{\vec{o}}^{(p)} + [\vec{i} - S \hat{\vec{o}}^{(p)}]. \quad (2.16)$$

Using  $\hat{\vec{o}}^{(0)} = \vec{i}$  as a starting point.

Another one is the method of point successive over-relaxation [14], where

$$\hat{o}_n^{(p+1)} = \hat{o}_n^{(p)} + \frac{\kappa}{S_{nm}} [i_n - \sum_{m < n} S_{nm} \hat{o}_m^{(p)} - \sum_{m \geq n} S_{nm} \hat{o}_m^{(p)}], \quad (2.17)$$

and the relaxation parameter  $\kappa$  can be adjusted to increase convergence.

All the linear methods share the same limitation: they cannot extrapolate beyond the data cutoff frequency. However, they can produce good results with a non-band limited data set. They are also a viable, efficient option in situations where computational speed is an issue.

### 2.2.3 Non-Linear Methods

These methods introduce non-linear operations in their algorithms using prior knowledge of the unknown object. Such is the case of the non-negative constraint for incoherent imaging, or the compact support constraint where the object is known to vanish outside a defined region. Through these constraints such methods can extrapolate beyond the data cutoff frequency.

One of these methods is Jansson's [14], [15], which takes advantages of both lower and upper bounds of the object. It was specially designed for spectroscopy (although it can be used in other fields) where transmittance is a non-negative quantity, and, in addition, is less than or equal to one. It is similar to the method of point successive over-relaxation (see eq. (2.17)) except that  $\kappa$  is defined as

$$\kappa(\hat{o}_n^{(p)}) = \kappa_o [1 - 2|\hat{o}_n^{(p)} - 1/2|]. \quad (2.18)$$

The dependence of  $\kappa$  upon  $\hat{o}_n^{(p)}$  is such that  $\kappa(\hat{o}_n^{(p)}) \rightarrow 0$  as either  $\hat{o}_n^{(p)} \rightarrow 0$  or 1. This constrains the output  $\hat{o}_n$  to the range  $0 \leq \hat{o}_n \leq 1$ .

In Frieden's maximum entropy method [15], the normalized object is modeled, by the law of large numbers, as a probability distribution. Then the principle of maximum entropy is applied [15], resulting in

$$H = - \sum_n \hat{o}_n \ln(\hat{o}_n) = \text{maximum}. \quad (2.19)$$

The noise in the image is also treated as an unknown array which has to be estimated. Using the Lagrange multiplier technique the following solution is obtained

$$\begin{aligned} \hat{o}_n &= \exp(-1 - \lambda_{M+1} - \sum_{m=1}^M \lambda_m S_{nm}), \\ \hat{n}_m &= \exp(-1 - \lambda_m/\rho) - B. \end{aligned} \quad (2.20)$$

The parameter  $\rho$  allows one to emphasize smoothness in  $\hat{\sigma}$  or  $\hat{n}$  (the larger  $\rho$ , the smoother the noise). The constant B is used to define a new set of non-negative noise

values  $N_m = n_m + B$ . The parameters  $\{\lambda_m\}$  are found by applying the solutions (3.30) to the constraint equations

$$\begin{aligned} S\hat{\sigma} + \hat{n} &= \vec{i}, \\ \sum_n \hat{\sigma}_n &= I_o, \end{aligned} \tag{2.21}$$

where  $I_o$  is the image total energy.

One of the advantages of this method is that the form of the solution guarantees a positive estimate.

Another non-linear method is called "alternating projections onto convex sets" (POCS) [14]. From a geometrical point of view, a set is convex if every line segment with endpoints in the set is totally contained in that set. The sets of all band-limited functions, all non-negative functions, all functions having a known maximum value, and all functions having finite extent, are examples of convex sets. If a function belongs to two or more convex sets, it can be estimated by sequential projection of a solution onto each of the sets in repeated cycles. POCS is particularly useful for regularizing ill-posed deconvolution problems (using prior knowledge of the object to impose a non-linear convex constraints on the solution set).

In general non-linear methods yield better results than linear methods [14], [15]. The use of non-linear constraints based on prior knowledge allow them to extrapolate beyond the data cutoff frequency, restoring details impossible to attain with their linear counterparts. However non-linear methods have the drawback of being more time consuming than linear methods in similar situations.

## 2.3 Ill-Posed Problems and Regularization Approaches

### 2.3.1 Ill-Posed Problems

It was in the early 1900s when J. Hadamard introduced the notion of the well-posed problem. Following Katsaggelos [16]

“A problem characterized by the equation

$$A\vec{x} = \vec{y} \quad (2.22)$$

where  $\vec{x} \in H_1$ ,  $\vec{y} \in H_2$  (both  $H_1$  and  $H_2$  denote Hilbert spaces) and  $A$  is a bounded linear operator, is defined to be well-posed provided the following conditions are satisfied:

- (i) for every element of  $\vec{y} \in H_2$  there exists a solution in the space  $H_1$ ;
- (ii) the solution is unique;
- (iii) the problem is stable on the spaces  $(H_1, H_2)$ , which means that the solution depends continuously on the data.

Otherwise the problem is ill-posed.”

Another related concept is well-posedness in the least-squares sense, introduced by Nashed [17], which states that  $A\vec{x} = \vec{y}$  is well-posed if for each  $\vec{y} \in H_2$  there exists a unique least-squares solution (of minimum norm), which depends continuously on the data.”

Many practical and scientific problems lead to ill-posed problems, which makes the study of this kind of problem far more important than mere academic curiosity.

### 2.3.2 Ill-Conditioned System of Equations

Consider a linear system of equations

$$M\vec{x} = \vec{y}, \quad (2.23)$$

with  $M$  a  $m \times n$  matrix,  $\vec{x}$  the unknown vector and  $\vec{y}$  the data vector. The rank of  $M$ , say  $k$ , is defined as the number of linearly independent rows of  $M$ . An ill-posed problem arises if the rank of  $M$  is less than the number of columns of  $M$  ( $k < n$ ), since for this case the solution is not unique.

A related concept is the so called ill-conditioned system of equations. For this a small perturbation in the data results in a large (although bounded) perturbation in the solution. In practice, due to the presence of noise in the input data and roundoff errors, it is not possible to determine whether a given system of equations is singular or ill-conditioned in all cases.

A useful tool to analyze ill-conditioned system of equations is the singular value decomposition (SVD). This allows one to decompose a matrix  $M \in \mathbb{R}^{m \times n}$  as the product of three matrices [18]

$$M = U \Sigma V^t = \sum_{i=1}^n u_i \sigma_i v_i^t, \quad (2.24)$$

where  $U = (\vec{u}_1, \vec{u}_2, \dots, \vec{u}_n) \in \mathbb{R}^{m \times n}$  and  $V = (\vec{v}_1, \vec{v}_2, \dots, \vec{v}_n) \in \mathbb{R}^{n \times n}$  are matrices with orthonormal columns, and  $\Sigma = \text{diag}(\sigma_1, \sigma_2, \dots, \sigma_n)$ . The numbers  $\sigma_i$  are called the "singular values" of  $M$ , they are non-negative and are ordered in non-increasing values ( $\sigma_1 \geq \sigma_2 \geq \dots \geq \sigma_n \geq 0$ ). The condition number of  $M$  can be computed using the first singular value  $\sigma_1$ , and the smallest non-zero singular value, say  $\sigma_k$  [18]

$$\text{cond}(M) = \frac{\sigma_1}{\sigma_k}. \quad (2.25)$$

If  $\sigma_k \ll \sigma_1$  the solution  $\vec{x}$  to the eq. (2.23) is very sensitive to perturbations of  $M$  and  $\vec{y}$ .

### 2.3.3 Regularization Approaches

Regularization of an ill-posed problem is the process through which an appropriate solution is found that is stable under small changes of the input data. Regularization approaches include one or more of the following intuitive ideas [16]

- (a) change of the concept of a solution;
- (b) restriction of the data;
- (c) change of the space and/or topologies;

- (d) modification of the operator itself;
- (e) the concept of regularization operators; and
- (f) well-posed stochastic extensions of ill-posed problems.

In order to apply these ideas, supplementary information about the true solution is used, for example, knowledge that the true solution is non-negative, or bounded, or non-zero over a finite region, etc.

### 2.3.4 Least-Squares Solution

Frequently, a greater number of measurements than unknowns is taken in order to reduce the effect of measurement errors. This makes eq. (2.23) an overdetermined system of equations. An overdetermined system of equations is, in general, not consistent, this leads to the necessity of defining an approximation criterion to solve it. A very common choice is the least-squares criterion [19], [20], which minimizes the 2-norm of the residual vector, that is:

$$\min_{\vec{x}} \|M\vec{x} - \vec{b}\|. \quad (2.26)$$

Numerous methods exist for solving the least-squares problem. One of them uses QR decomposition of the matrix  $M$  [19], [20], [21], [22]. The QR decomposition method has the advantage of stability with regard to propagating data errors [19], [20], [21]. It consists of the decomposition of the matrix  $M$  into the product of an orthogonal matrix  $Q$  and an upper-triangular matrix  $R$ , i.e.

$$M = QR. \quad (2.27)$$

Then an upper-triangular system is formed:

$$R\vec{x} = Q^t\vec{b}, \quad (2.28)$$

( $Q^t$  is the transpose of  $Q$ ), and solved by back substitution [20], [21], [22].

Among the different methods used to form the QR decomposition, the Householder transformation stand out because of its effectiveness [19], [20]. A householder transformation associated with a unit vector  $\hat{e}$  is defined as [22], [23]:

$$T = I - 2\hat{e}\hat{e}^t, \quad (2.29)$$

where  $I$  is an identity matrix. The matrix  $T$  is symmetric and orthogonal. By applying a suitable sequence of Householder transformation to a matrix  $M$ , it is possible to transform such matrix into a upper-triangular matrix  $R$  [22], [23]. The orthogonal matrix  $Q$  is just the transpose of the multiplication of the Householder transformation matrices applied to  $M$ . The Householder transformation method requires less storage location than other techniques used to solve the least-squares problem [19] (modified Gram-Schmidt orthogonalization, use of the normal equation, for example). This compact storage feature makes the Householder transformation a convenient technique in solving the least-squares problem when  $M$  is a large matrix.

Sometimes, the least-squares solution  $\vec{x}$  is subject to a set of linear constraints For this case the problem can be formulated as [20], [24]:

$$\min_{\vec{x}} \left\| M\vec{x} - \vec{b} \right\|, \quad \text{subject to } C\vec{x} = \vec{g}. \quad (2.30)$$

where  $C$  is a  $p \times n$  matrix,  $p < n$ . The solution is found by first solving the under-determined system of equations  $C\vec{x} = \vec{g}$ , and then transforming the problem into an unconstrained least-squares problem of minimizing  $\left\| M'\vec{x} - \vec{b}' \right\|$  [20].

In many practical problems some of the equations forming the linear system of equations (2.23) are more accurate than others. One way to deal with this is to weigh the accurate equations heavily and solve the resulting least-squares problem [19], [25], [26], i.e., finding the solution to the following minimization problem:

$$\min_{\vec{x}} \left\| W(M\vec{x} - \vec{b}) \right\|, \quad (2.31)$$

where  $W$  is a diagonal matrix, with diagonal elements  $w_i$  equal to the weight factor of the  $i^{\text{th}}$  equation.

## 2.4 Imaging Through a Turbulent Medium

### 2.4.1 Atmospheric Turbulence

As it was stated in Chapter 1, atmospheric turbulence imposes strong limitations in the resolution achieved by terrestrial telescopes. For example a 5 *m* telescope has a diffraction limited angular resolution (this would be the angular resolution of the telescope if it would be aberration and atmosphere free) of approximately 0.02 *arc seconds*, at a mean wavelength of 400 *nm*, while the angular resolution for a long-exposure image is approximately 1 *arc second* in good seeing [1].

Large scale refractive index inhomogeneities are caused by the non-uniform heating of the Earth's surface. These are broken up to smaller sizes by turbulent wind flow. These refractive index inhomogeneities are random in nature, and it is necessary to use random process theory to study them.

One of the most important statistical properties of a random process is the power spectral density  $\Phi(\vec{k})$ , which is the three-dimensional F.T. of the spatial autocorrelation function [27], [28]. For homogeneous turbulence  $\Phi(\vec{k})$  may be regarded as a measure of the relative abundance of packets of air, each with a characteristic refractive index, with dimensions  $L_1 = 2\pi/k_1$ ,  $L_2 = 2\pi/k_2$ , and  $L_3 = 2\pi/k_3$ .

From Kolmogorov's work [27] the power spectrum of the refractive index fluctuations, for the case of isotropic turbulence, is given by

$$\Phi(k) = 0.033C_n^2 k^{-11/3}. \quad (2.32)$$

The parameter  $C_n^2$  is the index structure constant, and measures the strength of the refractive index fluctuations. It depends on both local atmospheric conditions and height above ground. A typical average value for  $C_n^2$  is  $10^{-15} \text{meter}^{-2/3}$ .

Another useful parameter is Fried's parameter  $r_o$ . It provides a measure of the coherence diameter of the atmosphere [27]. Using Fried's parameter Kolmogorov's power spectrum takes the form [29]

$$\Phi(\xi) = \frac{0.023}{r_o^{5/3} \xi^{11/3}}. \quad (2.33)$$

We have used a linear spatial frequency  $\xi$  instead of a angular spatial frequency  $k$  ( $k = 2\pi\xi$ ). Values for  $r_o$  might range from 5 *cm* under condition of poor seeing to 20 *cm* under condition of exceptionally good seeing [27].

#### 2.4.2 Long- and Short-Exposure Pictures

Instantaneous wavefront degradation fluctuates rapidly with time due to the constant turbulent motion of the atmosphere's inhomogeneities. To avoid any time averaging effects, a exposure time of 0.01 *sec* or less is used. This effectively "freezes" the atmospheric turbulence, resulting in a temporarily constant, but random function across the telescope pupil. A typical short exposure picture of an unresolved star has a speckle-like structure. It is an experimental result that the speckle "size" is of the same order of magnitude as the Airy disc of the telescope [1].

On the contrary a long exposure picture (a picture taken with an integration time much greater than 0.01 *sec*) presents a smooth intensity distribution, since the latter is the average of many realizations of short exposure pictures. This average causes the long exposure pictures to lose the information that is present at high spatial frequencies.

For each short exposure picture eq. (2.2) applies, since the atmospheric turbulence is practically frozen during the exposure time. In general the PSF for this case is shift-variant due to the fact that the wavefronts from two points separated by some angular distance do not pass through identical parts of the atmosphere. However for pictures covering a small angular distance the PSF can be considered, to a good

approximation, shift-invariant. It has been observed that the isoplanatic patch size is of the order of 4 *arc seconds*. Therefore inside the isoplanatic patch (2.4) applies.

Figure 2.1 shows a pictorial model of the image formation of a point source through the atmosphere.

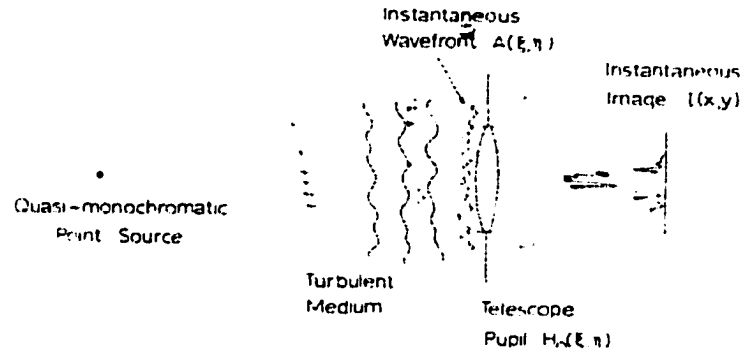


FIGURE 2.1. Image formation of a point source through the atmosphere

The instantaneous transfer function  $\tau(\vec{k})$  is given by the space autocorrelation of the pupil function  $H(\vec{\zeta})$  [1]

$$\tau(\vec{k}) = \int_{-\infty}^{\infty} \int_{-\infty}^{\infty} d^2\vec{\zeta}' H^*(\vec{\zeta}') H(\vec{\zeta}' + \vec{\zeta}). \quad (2.34)$$

The components of  $\vec{\zeta}$  are distances in the pupil and are related to the spatial frequency variables by  $\zeta_1 = \lambda f k_1 / 2\pi$ ,  $\zeta_2 = \lambda f k_2 / 2\pi$ , where  $\lambda$  is the wavelength of the point source and  $f$  is the focal length.

Because of atmospheric turbulence, the pupil function is equal to the product of the pupil function of the telescope  $H_o(\vec{\zeta})$  and the complex amplitude  $A(\vec{\zeta})$  due to the light from a point source that is propagated through the atmosphere [1]

$$H(\vec{\zeta}) = A(\vec{\zeta}) H_o(\vec{\zeta}). \quad (2.35)$$

The long exposure transfer function  $\tau_L(\vec{k})$  is the ensemble average (assuming ergodicity) of the instantaneous transfer function. Taking the average of eq. (2.34) it

is found that [27]

$$\tau_L(\vec{k}) = \tau_o(\vec{k})C_A(\vec{k}). \quad (2.36)$$

This states that the long exposure transfer function is equal to the product of the transfer function of the telescope  $\tau_o(\vec{k})$  (which is the autocorrelation of  $H_o(\vec{\zeta})$ ) and the coherence function or transfer function of the atmosphere  $C_A(\vec{k})$  (which is the ensemble average autocorrelation of  $A(\vec{\zeta})$ ).

To get an expression for  $C_A(\vec{k})$ , a model for the probability distribution of  $A(\vec{\zeta})$  has to be adopted. A very realistic model is the log normal. It assumes that log amplitude and phase of  $A(\vec{\zeta})$  are independent Gaussian random variables. Using this model,  $C_A(\vec{k})$  takes the form [27]

$$C_A(\vec{k}) = \exp(-const \cdot k^{5/3}). \quad (2.37)$$

### 2.4.3 Computer Simulation of Atmospheric Turbulence

In order to computer-simulate images degraded by atmospheric turbulence, we have used the program written by Shaklan [29], which generates power spectrum for phase fluctuations. It uses a discrete version of eq. (2.33) for an array of  $N \times N$  pixels:

$$\Phi(\xi_m) = \frac{0.023N^{11/3}D^{5/3}}{N_D^{5/3}r_o^{5/3}\xi_m^{11/3}}, \quad (2.38)$$

with

$$\xi_m = \frac{m}{N\Delta x}, \quad m = 0, 1, \dots, N - 1, \quad (2.39)$$

where  $\Delta x$  is the spatial size of a pixel,  $D$  is the diameter of the telescope, which corresponds to  $N_D$  pixels in frequency space. The latter can be computed by using the diameter of the telescope, the wavelength  $\lambda$ , and the angular size of a pixel  $\alpha$  ( $\alpha = \Delta x/f$ ,  $f$  being the focal length of the optical system):

$$N_D = \frac{N\alpha D}{\lambda}. \quad (2.40)$$

## Chapter 3

# REGULARIZATION OF THE IMAGE DIVISION METHOD

### 3.1 Image Division Method

#### 3.1.1 Image Turbulence Problem

The image division approach starts with two short-exposure images ( $1/60$  s or less) of an incoherent object, which must be separated in time by more than one short-exposure duration ( $3/60$  s or more). The images result from two fixed, independent, turbulent phase distributions across the optical pupil. Assuming that both images have a sharp cutoff frequency  $\Omega$  in both directions would also entail their infinite extension. However, if they fall off to negligible values (compared with the inevitable noise of detection) for a certain  $|\vec{x}| > L/2$ , such images may now be truncated as to be contained inside a square of length  $L$ . Now, the Fourier transform of any of these images can be computed using eq. (2.5)

$$I(\vec{k})_{|k_1| \leq \Omega, |k_2| \leq \Omega} = \int_0^L \int_0^L d^2\vec{x} i(\vec{x}) \exp(-j\vec{k} \cdot \vec{x}). \quad (3.1)$$

For convenience the images are placed along the positive axes, which results in the integration limits shown above. The eq. (3.1) is an approximation since the image is truncated in spite of having infinite extension.

Because of the finite cutoff frequency of the image, we can use the Whittaker-Shannon sampling theorem, replacing eq. (3.1) by a discrete sum ([13])

$$I(\vec{k})_{|k_1| \leq \Omega, |k_2| \leq \Omega} = \sum_{m_1=0}^{M-1} \sum_{m_2=0}^{M-1} (\Delta x)^2 i(m_1\Delta x, m_2\Delta x) \exp(-j(m_1k_1 + m_2k_2)\Delta x), \quad (3.2)$$

allows us to express the term  $(m_1n_1 + m_2n_2)$  inside the exponent in eq. (3.7), as a function of  $m$  and  $n$

$$f(m, n) = m_1n_1 + m_2n_2. \quad (3.8)$$

Then eq. (3.7) simplifies to

$$I_n = (\Delta x)^2 \sum_{m=0}^{M^2-1} i_m \exp(-2\pi j f(m, n)/N^2). \quad (3.9)$$

Going back to the two-image scenario, and applying eq. (2.7) to both images (ignoring added noise of detection), we get

$$I_n^{(i)} = \tau_n^{(i)} O_n, \quad i = 1, 2; \quad n = 0, 1, \dots, N^2 - 1. \quad (3.10)$$

Forming the quotient of the image spectra

$$D_n \equiv \frac{I_n^{(1)}}{I_n^{(2)}} = \frac{\tau_n^{(1)} O_n}{\tau_n^{(2)} O_n} = \frac{\tau_n^{(1)}}{\tau_n^{(2)}}, \quad n = 0, 1 \dots N^2 - 1. \quad (3.11)$$

Note that the object spectrum  $O_n$  is canceled out in eq. (3.11), which eliminates one set of unknowns from the problem.

The transfer functions  $\tau^{(1)}$  and  $\tau^{(2)}$  are related to unknown PSF's  $s^{(1)}$  and  $s^{(2)}$ , by means of the sampling theorem, through expressions similar to eq. (3.9):

$$\tau_n^{(i)} = (\Delta x)^2 \sum_{m=0}^{M^2-1} s_m^{(i)} \exp(-2\pi j f(m, n)/N^2), \quad i = 1, 2. \quad (3.12)$$

Substituting eq. (3.12) into eq. (3.11) produces

$$D_n = \frac{\sum_{m=0}^{M^2-1} s_m^{(1)} \exp(-2\pi j f(m, n)/N^2)}{\sum_{m=0}^{M^2-1} s_m^{(2)} \exp(-2\pi j f(m, n)/N^2)}, \quad n = 0, 1, \dots, N^2 - 1. \quad (3.13)$$

In order to get a set of  $N^2$  equations, linear in the unknowns  $s^{(1)}$  and  $s^{(2)}$ , cross multiply eq. (3.13) and bring everything to one side

$$\sum_{m=0}^{M^2-1} (s_m^{(1)} - D_n s_m^{(2)}) \exp(-2\pi j f(m, n)/N^2) = 0, \quad n = 0, 1, \dots, N^2 - 1. \quad (3.14)$$

Now, since the data values  $D_n$  are generally complex, we can represent them using polar notation

$$D_n \equiv A_n \exp(2\pi j \phi_n / N^2), \quad (3.15)$$

where  $A_n$  and  $\phi_n$  are known modulus and phase values.

Separating the real and imaginary parts of eq. (3.14), we get

$$\begin{aligned} \sum_m \left[ s_m^{(1)} \cos \left( \frac{2\pi f(m, n)}{N^2} \right) - A_n s_m^{(2)} \cos \left( \frac{2\pi}{N^2} (\phi_n - f(m, n)) \right) \right] &= 0, \\ \sum_m \left[ s_m^{(1)} \sin \left( \frac{2\pi f(m, n)}{N^2} \right) - A_n s_m^{(2)} \sin \left( \frac{2\pi}{N^2} (\phi_n - f(m, n)) \right) \right] &= 0 \end{aligned} \quad (3.16)$$

These are  $2N^2$  linear equations in the  $2M^2$  unknowns  $s^{(1)}$  and  $s^{(2)}$ .

### 3.1.2 Overcoming the Homogeneity Problem

The eqs. (3.16) are homogeneous (the right hand sides are equal to zero), which poses a problem since the trivial solution ( $s_m^{(1)} = s_m^{(2)} = 0, m = 0, \dots, M^2 - 1$ ) will appear every time we attempt to solve this set of equations.

As we can see from eq. (3.13), the PSF solutions are invariant to multiplication by a constant. Now, if the PSF's are initially incorrect by such a factor, then the object solution (the goal of the solving process) is incorrect by the reciprocal of that factor. But this is an acceptable shortcoming since images are adjusted in absolute brightness for the viewers convenience. This means that we may assume any convenient value for the total energy  $E^{(1)}$  of  $s^{(1)}$ . The total energies for  $s^{(1)}$  and  $s^{(2)}$  are defined by

$$E^{(i)} \equiv \sum_m s_m^{(i)}, \quad i = 1, 2. \quad (3.17)$$

Solving eq. (3.17) for any one  $s_k^{(1)}$  value, say,

$$s_k^{(1)} = E^{(1)} - \sum_{m \neq k} s_m^{(1)}. \quad (3.18)$$

This allows us to remove  $s_k^{(1)}$  from the left-hand sums in eqs. (3.16), producing a nonzero right-hand side. Doing that yields the following equations:

$$\begin{aligned} & \sum_{m \neq k} \left[ s_m^{(1)} \cos \left( \frac{2\pi f(m, n)}{N^2} \right) - A_n s_m^{(2)} \cos \left( \frac{2\pi}{N^2} (\phi_n - f(m, n)) \right) \right] \\ &= -E^{(1)} \cos \left( \frac{2\pi f(k, n)}{N^2} \right) \end{aligned} \quad (3.19)$$

$$\begin{aligned} & \sum_{m \neq k} \left[ s_m^{(1)} \sin \left( \frac{2\pi f(m, n)}{N^2} \right) - A_n s_m^{(2)} \sin \left( \frac{2\pi}{N^2} (\phi_n - f(m, n)) \right) \right] \\ &= -E^{(1)} \sin \left( \frac{2\pi f(k, n)}{N^2} \right). \end{aligned} \quad (3.20)$$

Index  $n = 0, 1, \dots, N^2 - 1$  in eq. (3.19) and  $n = 1, \dots, N^2 - 1$  in eq. (3.20) (for  $n = 0$  it becomes the tautology  $0 = 0$  and, so, is skipped). Then they are  $2N^2 - 1$  linear equations in the  $2M^2 - 1$  unknowns. However  $N^2 - 1$  of these equations are found to be repetitions and so are ignored. This leaves, then,  $N^2$  equations in the  $2M^2 - 1$  unknowns. Making  $N^2 > 2M^2$  allows to form an overdetermined problem (more equations than unknowns).

The eqs. (3.19) and (3.20) take the convenient matrix form

$$H\vec{x} = \vec{b}, \quad (3.21)$$

where  $\vec{x}$  designates the vector of unknowns  $s_m^{(1)}$  and  $s_m^{(2)}$ ,  $H$  denotes the matrix of trigonometric coefficients in eqs. (3.19) and (3.20) and  $\vec{b}$  denotes the vector right-hand sides of eqs. (3.19) and (3.20).

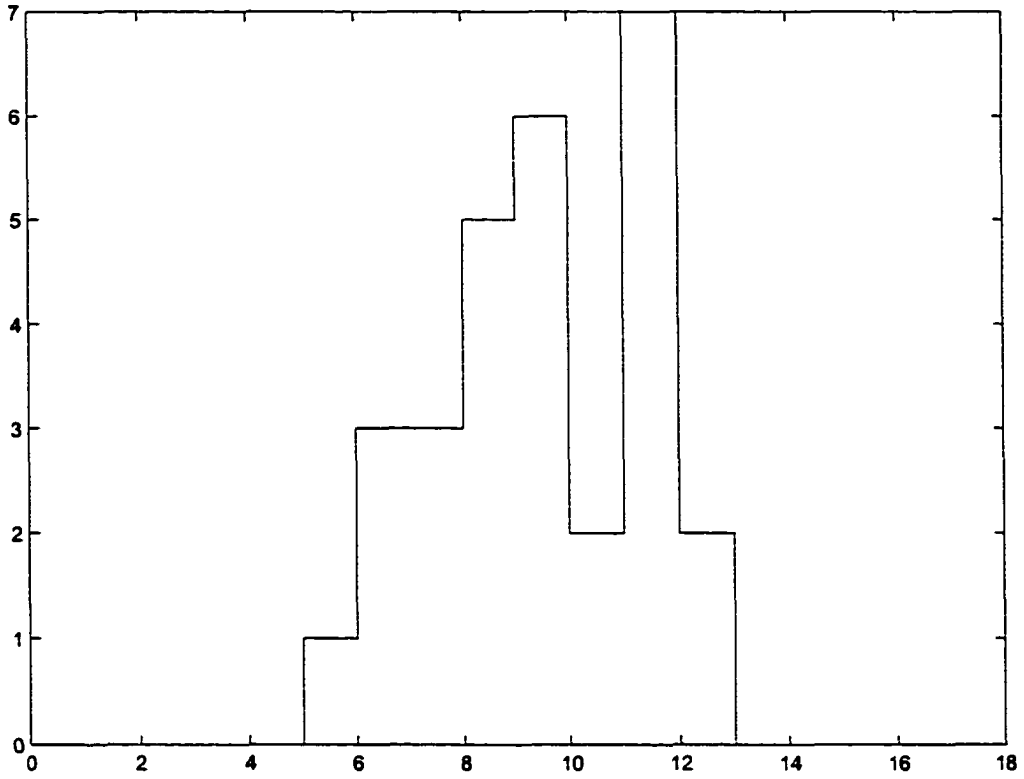


FIGURE 3.1. One-dimensional, eight pixels wide arbitrary object

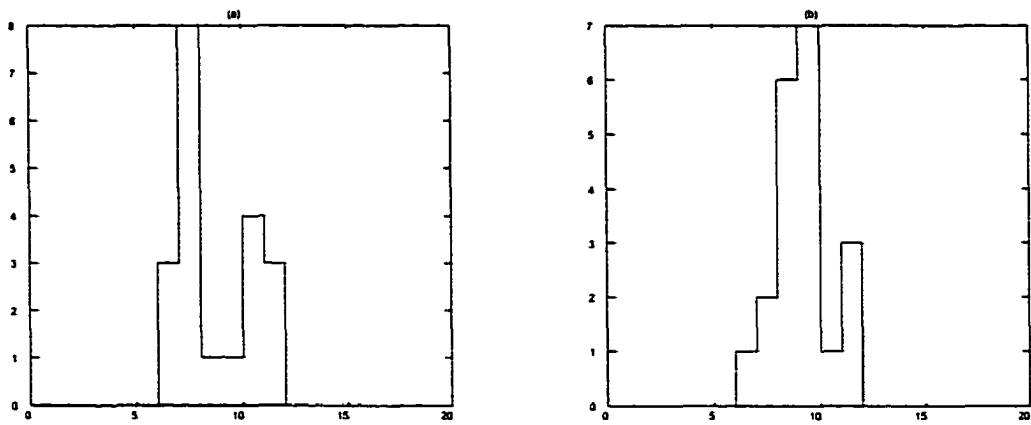


FIGURE 3.2. Two one-dimensional arbitrary PSF's. (a)  $s^{(1)}$ . (b)  $s^{(2)}$ .

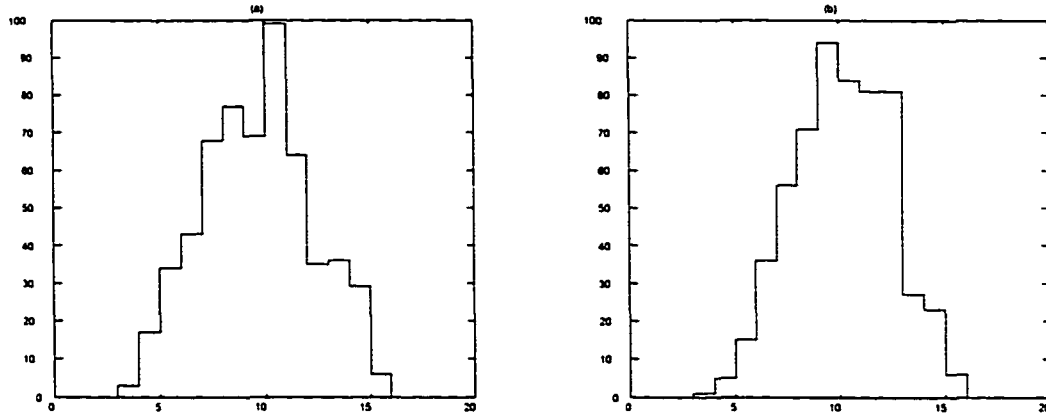


FIGURE 3.3. Resulting two different images. (a)  $i^{(1)}$ , (b)  $i^{(2)}$ .

16 pixels is imposed to the PSF's, the number of unknowns is reduced by just setting to zero the elements of the PSF's outside of the specified support, and a different solution is yielded. Figure 3.4 shows the solutions found for  $s^{(1)}$ , for different support situations, starting from 14 pixels to 2 pixels, with a reduction of 2 pixels per trial.

From Figure 3.4 it is possible to observe that a different solution for  $s^{(1)}$  is found for each given support (and well as for  $s^{(2)}$  and the object  $o$ ). The reconstructed PSF 1 for the support of 6 pixels (which is the original support of  $s^{(1)}$ ), case (f), merits special attention since it is an exact replica of the original PSF 1.

From this example we can reach the following conclusions. For noiseless data: 1) there is no unique solution to eqs. (3.19) and (3.20). This is expressed by the matrix  $H$  being rank deficient. 2) Different solutions are found by imposing different support to the PSF's. 3) The matrix  $H$  becomes full rank when the trial support equals the original support of the PSF's. 4) The desired solution is found for the latter case.

For a more realistic case of noisy data, the problem of rank deficiency for  $H$  is effectively resolved, due to the lack of invariance of data  $D_n$  under multiplication of both transfer functions  $\tau_n^{(1)}$  and  $\tau_n^{(2)}$  by an arbitrary function. This lack of invariance arises because, with data noise present in the image,  $D_n$  is no longer equal to the quotient of transfer functions  $\tau_n^{(1)}/\tau_n^{(2)}$ . In essence, the noise breaks the ambiguity.

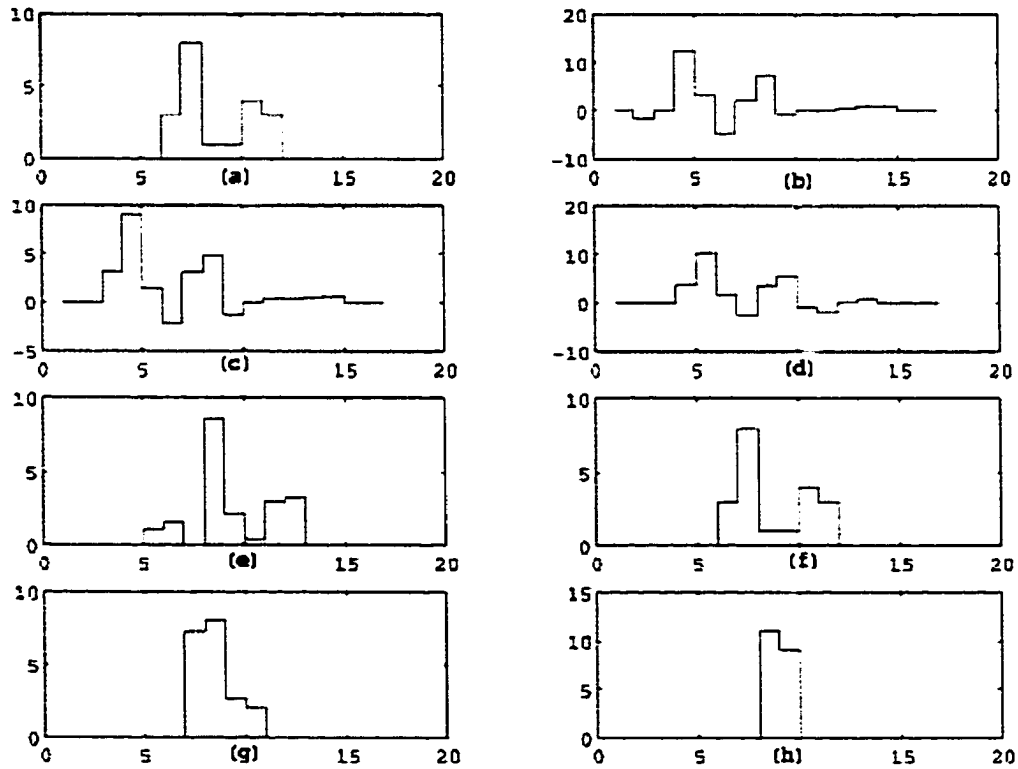


FIGURE 3.4. Reconstructed PSF 1 for different supports. (a) True  $s^{(1)}$ , (b) reconstructed  $s^{(1)}$  for 14 pixels support, (c) for 12 pixels supp., (d) for 10 pixels supp., (e) for 8 pixels supp., (f) for 6 pixels supp., (g) for 4 pixels supp., (h) for 2 pixels supp.

### 3.2.2 Least-Squares Solution

As we stated above the number  $N^2$  of data frequencies can be made arbitrary large. Making  $N^2 > 2M^2$  produces an overdetermined system of equations, which allows us to solve eq. (3.21) using a least-squares method. A least-squares method finds the solution  $\vec{x}$  that minimize the error metric  $\|H\vec{x} - \vec{b}\|$ , that is

$$\min_{\vec{x}} \|H\vec{x} - \vec{b}\|. \quad (3.22)$$

A least-squares solution is beneficial because it effects a degree of data noise smoothing, i.e., regularization, on its own.

In order to find a least-squares solution to eq. (3.22) we use a QR decomposition of matrix  $H$ . This factorization expresses the matrix  $H$  as the product of an orthogonal matrix and an upper-triangular matrix [31]. The QR decomposition is computed using the Householder transformation method [22], [23], [31]. The QR decomposition allows us to transform the problem into an upper-triangular system of equations which is solved by backsubstitution.

### 3.2.3 Prior Knowledge

The problem of solving eqs. (3.19) and (3.20) is ill-posed, because the lack of uniqueness of solution [16]. We need a regularization approach, in order to solve eqs. (3.19) and (3.20). Using prior knowledge of the unknowns, it is possible to produce a certain degree of regularization [14] For this problem it is possible to use two forms of prior knowledge [9]. One is positivity of the object and the PSF's. Since the images are incoherent, the object and the PSF's represent energy distributions, and therefore must obey a condition of positivity:

$$o_m \geq 0, \quad s_m^{(1)} \geq 0, \quad s_m^{(2)} \geq 0. \quad (3.23)$$

The other form of prior knowledge is the finiteness of support for the PSF's and the object. Both the object and the PSF's are, effectively zero outside regions of finite extension. Also consider only a case in which these extensions are small enough that the image field contains all the image energy: none of it spills outside of the field. The compact support of the PSF's can be incorporated as a constraint. This makes the problem a constrained least-squares problem, that is:

$$\min_{\vec{x}} \left\| H\vec{x} - \vec{b} \right\|, \quad \text{subject to } P\vec{x} = \vec{0}, \quad (3.24)$$

where  $P$  is the Projection operator into the subspace spanned by the vectors  $\vec{x}$  outside the compact support of the PSF's.

### 3.2.4 Net Algorithm

A fixed-length restoration approach can be developed on the basis of the above considerations. If the correct support for the PSF's  $K_{x_1}$  and  $K_{x_2}$  were known, the approach would be simply the preceding least-squares method. However for real data this is not the case. Now, if we solve eq. (3.21) using the least-squares method for a fixed sequence of trial values  $\hat{K}_{x_1}$  and  $\hat{K}_{x_2}$ , the "correct" solution would be among the found solutions (assuming that the correct PSF's support are among the trial values). We will just need a criterion to select it. The latter can be built up using prior knowledge of the object and PSF's as follows. Enforcing positivity and support consistency over each solution (on the PSF's estimates and correspondent object estimate), the best solution is defined to be the one that gives a pair of image estimates that best agree with the two given images. Below, the algorithm is presented as a series of steps, and also shown schematically in Figure 3.5.

(1) The primary data for the problem is given as a pair of short-exposure images  $i^{(1)}$  and  $i^{(2)}$ . Spectra  $I^{(1)}$  and  $I^{(2)}$ , from these images, are formed by a discrete Fourier transform, eq. (3.9). Then quantities  $D_n$  are computed by dividing  $I_n^{(1)}$  over  $I_n^{(2)}$ , as

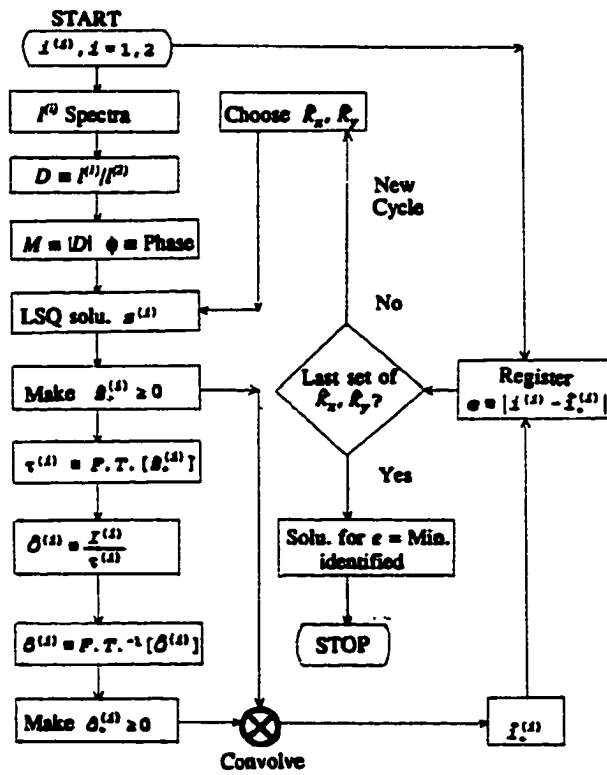


FIGURE 3.5. Flow chart for the image division program.

in eq. (3.11), and represented in polar notation, from where the modulus and phase quantities  $M_n$ , and  $\phi_n$  are obtained. The latter may be regarded as secondary (i.e., preprocessed) data for the problem.

(2) The quantities  $M_n$ , and  $\phi_n$  are used to form eqs. (3.19) and (3.20), which we will attempt to solve by a least-squares approach.

(3) A support choice for both PSF's is made, say  $\hat{K}_{x_1}$  and  $\hat{K}_{x_2}$ . These are smaller than the total image field extension. This choice is imposed on eqs. (3.19) and (3.20) by setting to zero all the components of  $s^{(1)}$  and  $s^{(2)}$  outside the estimate support region, reducing the unknowns  $\vec{x}$  in problem (3.24).

(4) The least-squares solution  $\vec{x}_{LSQ} \equiv (\hat{s}^{(1)}, \hat{s}^{(2)})^t$  to problem (3.22) is formed by use of QR factorization [31]. This factorization avoids the need to take matrix inverses, a numerically unstable operation for poorly conditioned matrices. The outputs  $\hat{s}^{(1)}$  and  $\hat{s}^{(2)}$  are forced to obey positivity by replacing all negative values by zero. These are the estimated PSF's  $\hat{s}_+^{(1)}$  and  $\hat{s}_+^{(2)}$ .

(5) The estimated transfer functions  $\hat{\tau}^{(1)}$  and  $\hat{\tau}^{(2)}$  are computed by Fourier transforming the estimated PSF's from the prior step. Then they are used in eq. (3.10) to form object spectrum estimates:

$$\hat{O}_n^{(i)} \equiv I_n^{(i)} / \tau_n^{(i)}, \quad i = 1, 2. \quad (3.25)$$

by inverse filtering.

(6) The inverse-Fourier transform of these estimates are taken to yield object estimates  $\hat{o}^{(i)}$ ,  $i = 1, 2$ .

(7) Positivity is enforced upon these object estimates by setting to zero every negative value.

(8) Support consistency is also enforced, as follows. For a one-dimensional discrete case, it is known that if  $f_1$ ,  $f_2$  and  $f_3$  are related by the convolution operation (i.e.,  $f_1 = f_2 \odot f_3$ ) then their supports are related by the equation

$$K_1 = K_2 + K_3 - 1. \quad (3.26)$$

Similarly for a two-dimensional case eq. (3.26) applies for both directions. Now, defining (for example) the  $x_1$ -component support  $K_{imx}$  in the image as its linear extension at the 2% level of maximum intensity, and with the trial value  $\hat{K}_x$  as the  $x_1$ -component support of the PSF's, the  $x_1$ -component support  $\hat{K}_{obx}$  of the object is found by using eq. (3.26)

$$\hat{K}_{obx_1} = K_{imx_1} - \hat{K}_{x_1} + 1. \quad (3.27)$$

The estimated object is zeroed outside this support interval. For the  $x_2$ -component direction the same procedure is performed.

(9) The convolution is taken of each estimated PSF from step (4), with a corresponding object estimate from step (8). This yields estimated images

$$\hat{i}_+^{(i)} \equiv \hat{s}_+^{(i)} \odot \hat{o}_+^{(i)}, \quad i = 1, 2. \quad (3.28)$$

(10) These estimated images are compared to the given images  $i^{(1)}$  and  $i^{(2)}$  to define the validity of the hypothetical support values in step (3). To measure the inconsistency of the solution with the image data, an error metric over both images is formed:

$$e \equiv \frac{e^{(1)} + e^{(2)}}{2}, \quad e^{(i)} \equiv \frac{|i^{(i)} - \hat{i}_+^{(i)}|}{|i^{(i)}|}. \quad (3.29)$$

In this way the inconsistency is quantified. Its size is used to indicate whether the support values are correct.

(11) The value of  $e$  is registered, and a new cycle begins at step (3), with a new choice of supports.

(12) After finishing the cycle from step (3) to (11) for every choice of supports the rendered  $e$  values are compared to find the minimum of them, which identifies the

final solution  $\hat{s}_+^{(i)}, \hat{o}_+^{(i)}, i = 1, 2$ . The arithmetic average of the two object estimates defines the output object:

$$\hat{o} \equiv \frac{(\hat{o}_+^{(1)} + \hat{o}_+^{(2)})}{2}. \quad (3.30)$$

## Chapter 4

# DEMONSTRATIONS

In this chapter the effectiveness of the image division algorithm is tested through use of both computer simulations and real images. Data processing was made with a desktop computer with a 1.9 GHz Pentium IV processor, and 512 MB of RAM memory. MATLAB version 6.0.1 was used to process the examples. Comparisons to the results shown by Ayers and Dainty's method [9], Lane's method [10] and Holmes method [12] are also given.

### 4.1 Simulation Data

In order to test the image division algorithm in several scenarios, simulation examples are presented for different kind of objects (a binary star system, a cluster of stars and a galaxy), different levels of atmospheric turbulence (low  $r_0 = 0.2$  m, moderate  $r_0 = 0.1$  m and high  $r_0 = 0.05$  m), and different levels of additive noise (1%, 3%, 5%, 8% and 10%). The latter is independent Gaussian, with a standard deviation  $\sigma$  that is expressed as a % of the root-mean-square (r.m.s.) signal level. A  $64 \times 64$  pixel array is used for the images. The image spectral field size in all cases is  $90 \times 90$  frequencies, or  $N = 8100$ , this allows to stretch the search for the PSF's supports up to  $63 \times 63$  pixels keeping  $N > 2M$ . (Larger field sizes might require the use of a mainframe computer). Limits on the PSF's support search were set as follows: for the low turbulence cases  $K_1$  was allowed to vary from 16 to 35 pixels, for the moderate turbulence cases from 31 to 50 pixels, and for the high turbulence cases from 50 to 63 pixels. For each value of  $K_1$  five different values for  $K_2$  were allowed ( $K_1$ ,  $K_1 \pm 1$ ,  $K_1 \pm 2$ ). Therefore each case required 100 (or 70 for the high turbulence cases) cycles [steps (2)-(11)] of the algorithm. On average the execution time for each of these



FIGURE 4.1. Two short-exposure images of a binary star system, for low turbulence  $r_0 = 0.2 m$ , no noise added case. (a) Image 1, (b) image 2.

cycles was  $\sim 5$  min, this represents a total time of  $\sim 500$  min for each case.

#### 4.1.1 Binary star system

*a) Low turbulence, zero noise:* For the first case a binary star system is used. The stars are separated by  $0.2$  arc seconds (4 pixels). The dim star has a brightness which is about 40% of that of its neighbor sister. See Figure 4.2(a). Two turbulent degraded PSF's were generated using eq.(2.38), see Figures 4.3(a) and 4.3(b). The parameters were set as follows:  $N = 64$ ,  $\lambda = 550 nm$ ,  $D = 5 m$ ,  $\alpha = 0.02$  arc seconds,  $r_0 = 0.2 m$ , the last represents a low turbulence case. These PSF's are mathematically convolved with the binary-star object to form two short-exposure images of the stars (see Figure 4.1). No noise was added for this case. Notice how turbulence degrades the images, making it impossible to distinguish clearly the binary system.

The images were used as inputs to the regularized image division method. Reconstruction of the binary star system is given in Figure 4.2(b). It is possible to observe that for this noiseless case the reconstruction is excellent. The reconstructed PSF's



FIGURE 4.2. A binary star system. The stars are separated by  $0.2$  arc seconds (4 pixels). The dim star has a brightness which is about 40% of that of its neighbor sister (a) Original object. (b) Reconstruction for low turbulence  $r_o = 0.2$  m, no noise added case.

are shown, respectively, in Figures 4.3(c) and 4.3(d)

(b) *High turbulence, 1% of additive Gaussian noise* Using the same object, the binary stars, two PSF's are generated for high turbulence case,  $r_o = 0.05$  m, see Figures 4.6(a) and 4.6(b). These PSF's are convolved with the binary-star object, and 1% Gaussian noise is added to form two short-exposure images. The latter are shown in Figures 4.4(a) and 4.4(b).

The reconstructed object is shown in Figure 4.5(b). Compare this reconstruction with the short-exposure images, Figures 4.4(a) and 4.4(b). This example allows us to claim effectiveness for the regularized image division approach even in the case of a high level of turbulence. The reconstructed PSF's are shown in Figures 4.6(c) and 4.6(d).

(c) *Low turbulence, 3% of additive Gaussian noise.* Using again the binary stars, and a high level of turbulence  $r_o = 0.05$  m, now we add 3% Gaussian noise. The two

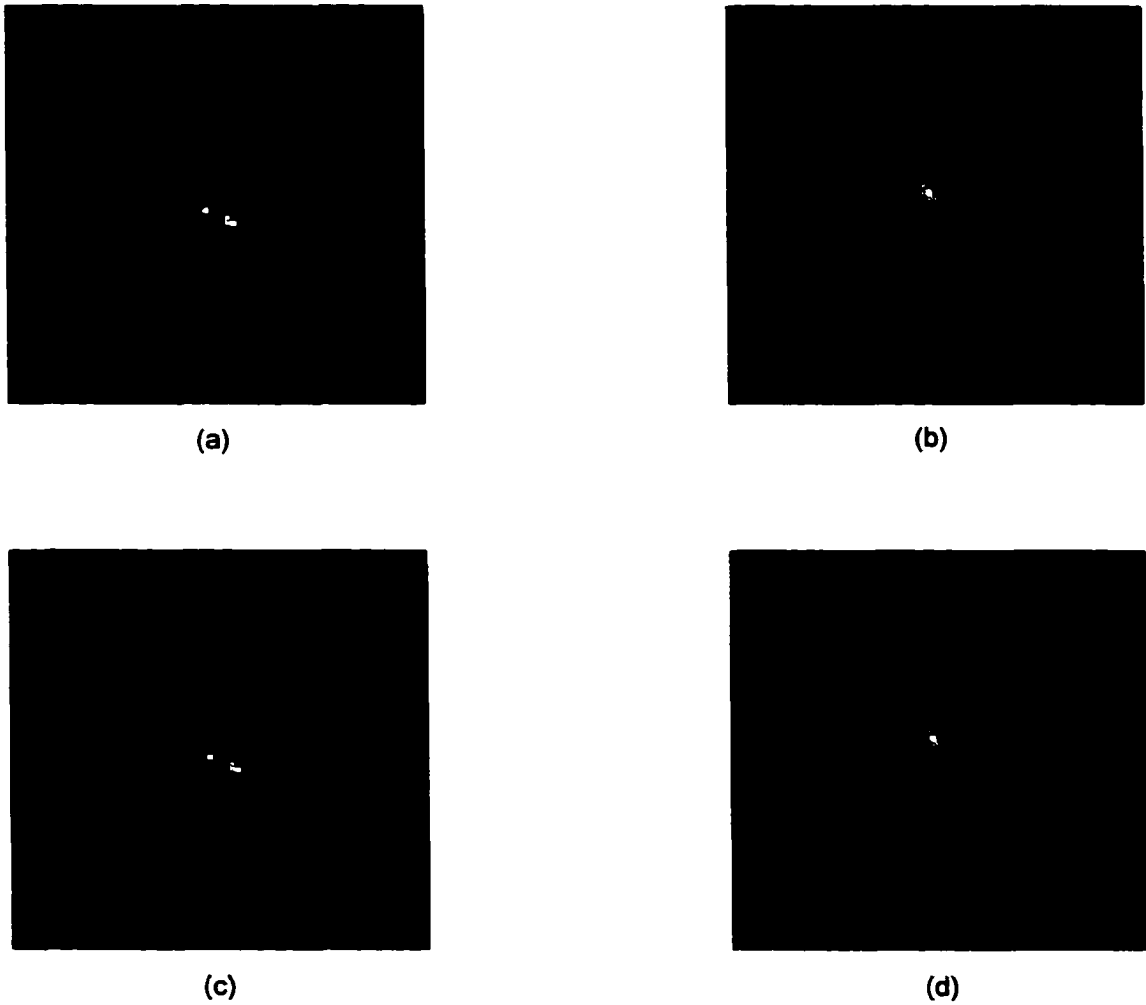


FIGURE 4.3. Two turbulent degraded PSF's, for the no added noise case. (a) PSF 1, (b) PSF 2, (c) Reconstructed PSF 1, (d) Reconstructed PSF 2.



FIGURE 4.4. Two short-exposure images of a binary star, for high turbulence,  $r_o = 0.05 m$ , 1% additive Gaussian noise case. (a) Image 1, (b) Image 2.



FIGURE 4.5. Binary stars, high turbulence  $r_o = 0.05 m$ , 1% additive Gaussian noise case. (a) Original object. (b) Reconstruction.

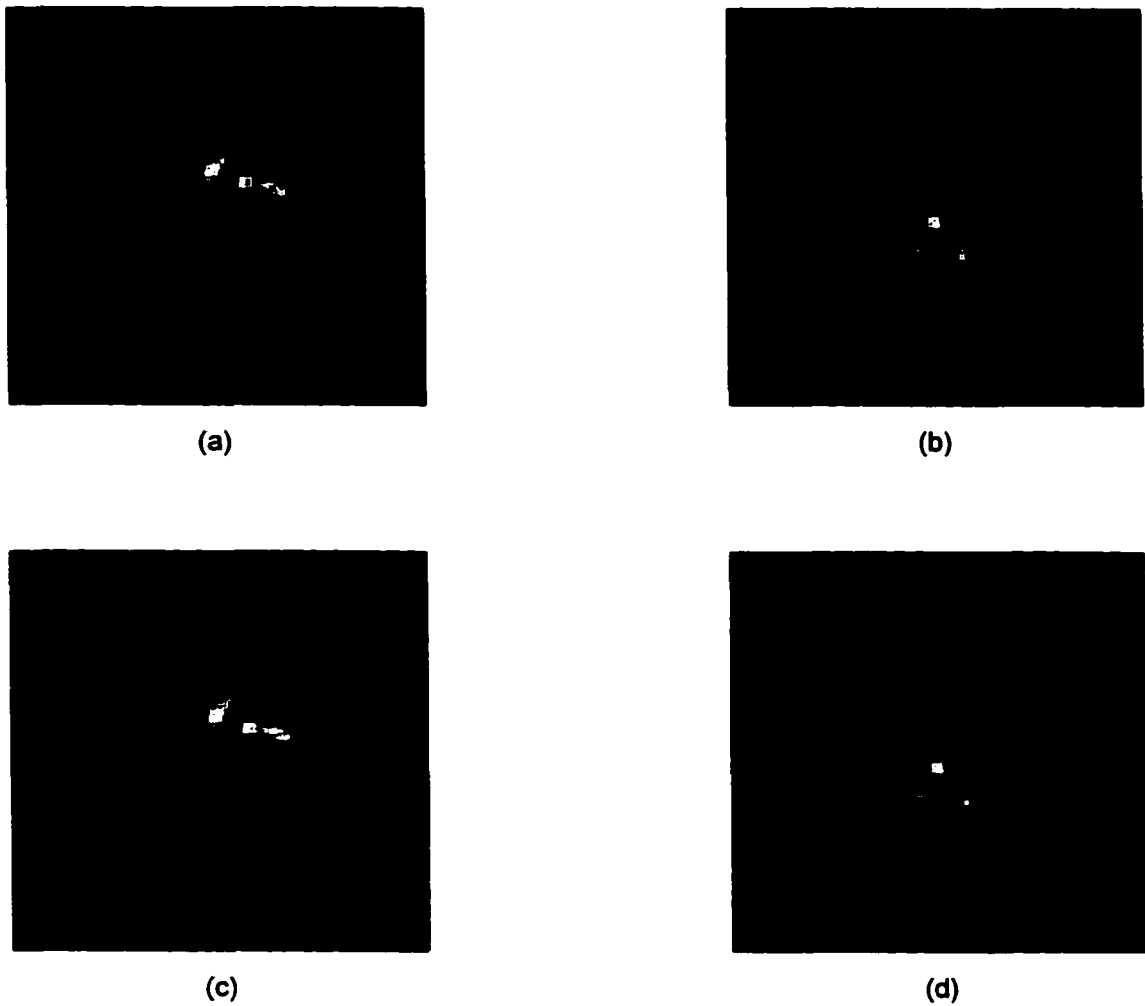


FIGURE 4.6. Two high-turbulent degraded PSF's,  $r_o = 0.05$  m, used for the 1% additive Gaussian noise case. (a) PSF 1. (b) PSF 2. (c) Reconstructed PSF 1. (d) Reconstructed PSF 2.



FIGURE 4.7. Two short-exposure images for high turbulence,  $r_o = 0.05 m$ , 3% additive Gaussian noise case. (a) Image 1. (b) Image 2.

short-exposure images are shown in Figures 4.7(a) and 4.7(b).

The reconstructed object for this case is shown in Figure 4.8(b). Observe that the reconstruction is still pretty good for this level of noise. The reconstructed PSF's are shown in Figures 4.9(c) and 4.9(d).

*(d) Low turbulence, 5% additive Gaussian noise.* The next case is for low level of turbulence  $r_o = 0.2 m$  and 5% additive Gaussian noise. The two images used as inputs are given in Figures 4.10(a) and 4.10(b).

Reconstruction of the object for this case is given in Figure 4.11(b). For this level of noise the reconstruction is still good, although spurious background details start appearing. The reconstructed PSF's are shown in Figures 4.12(c) and 4.12(d).

*(e) High turbulence, 8% additive Gaussian noise.* For this case the noise is increased to 8%, while the level of turbulence is high,  $r_o = 0.05 m$ . Two images are formed for this case, as given in Figures 4.13(a) and 4.13(b).

The reconstructed object for this case is given in Figure 4.14(b). Now it is possible



FIGURE 4.8. Binary star system, high turbulence,  $r_o = 0.05 m$ , 3% additive Gaussian noise case. (a) Original object. (b) Reconstructed object.

to observe that the reconstruction contains a great amount of spurious noise which makes the recognition of the binary stars a difficult task. The reconstructed PSF's are shown in Figures 4.15(c) and 4.15(d).

(f) *Low turbulence, 10% additive Gaussian noise.* The last case for the binary-star object is formed with a low level of turbulence,  $r_o = 0.2 m$ , and 10% additive Gaussian noise. The two images used as input are given in Figures 4.16(a) and 4.16(b).

The reconstructed object is shown in Figure 4.17(b). For this level of noise the reconstruction is so poor that it has little resemblance with the original object. The reconstructed PSF's are shown in Figures 4.18(c) and 4.18(d).

As a summary for the binary-star examples we can say that it is possible to obtain good reconstruction of objects, independent of the level of turbulence, for noise levels up to about 5%. Higher levels of noise yield reconstructions with an objectionable level of spurious background noise.



FIGURE 4.10. Short-exposure pictures of binary stars for a low level of turbulence,  $r_o = 0.2 m$ , and 5% additive Gaussian noise. (a) Image 1. (b) Image 2.



FIGURE 4.11. Binary stars. (a) Original object. (b) Reconstruction for a low level of turbulence,  $r_o = 0.2 m$ , and 5% additive Gaussian noise.

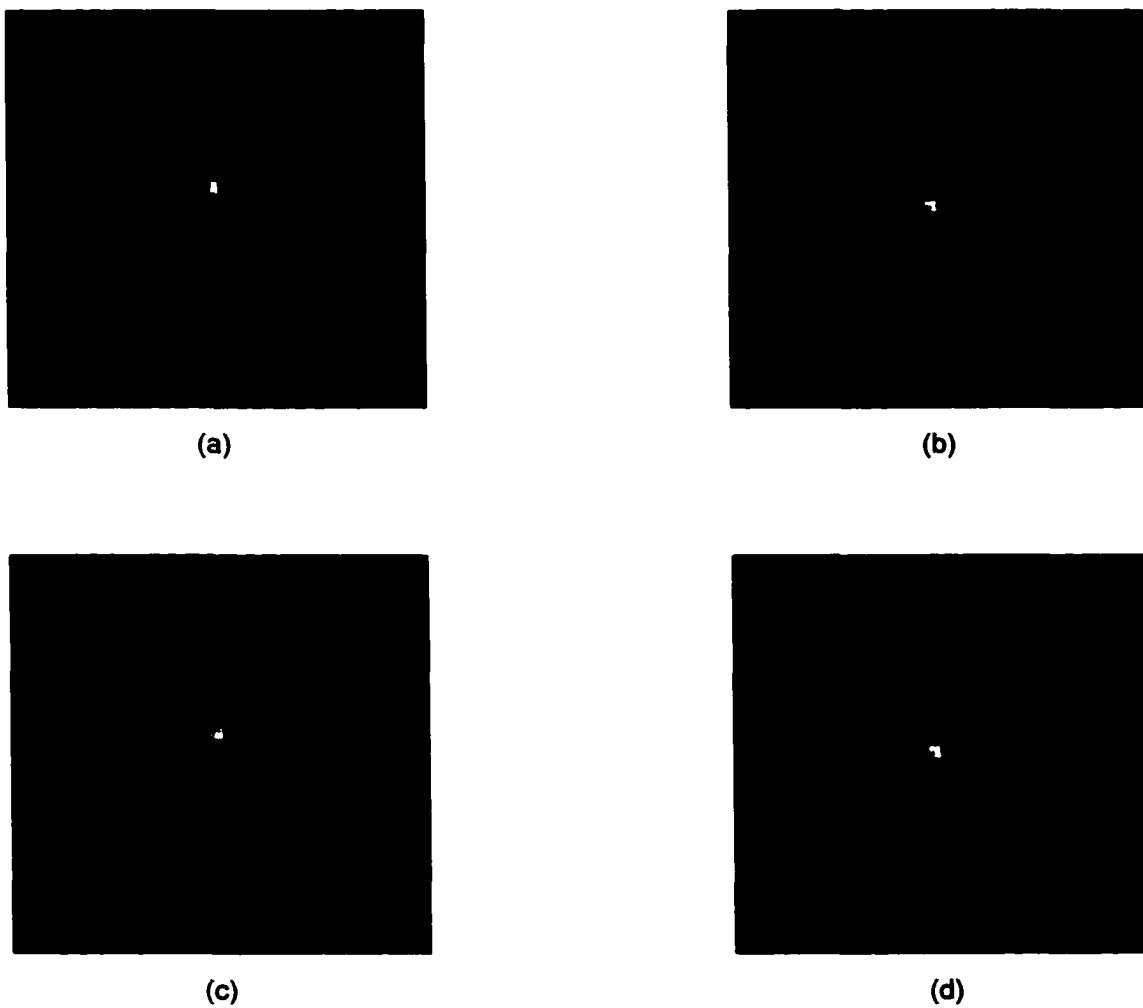


FIGURE 4.12. Low turbulent degraded PSF's, for a 5% additive Gaussian noise case. (a) PSF 1. (b) PSF 2. (c) Reconstructed PSF 1. (d) Reconstructed PSF 2.

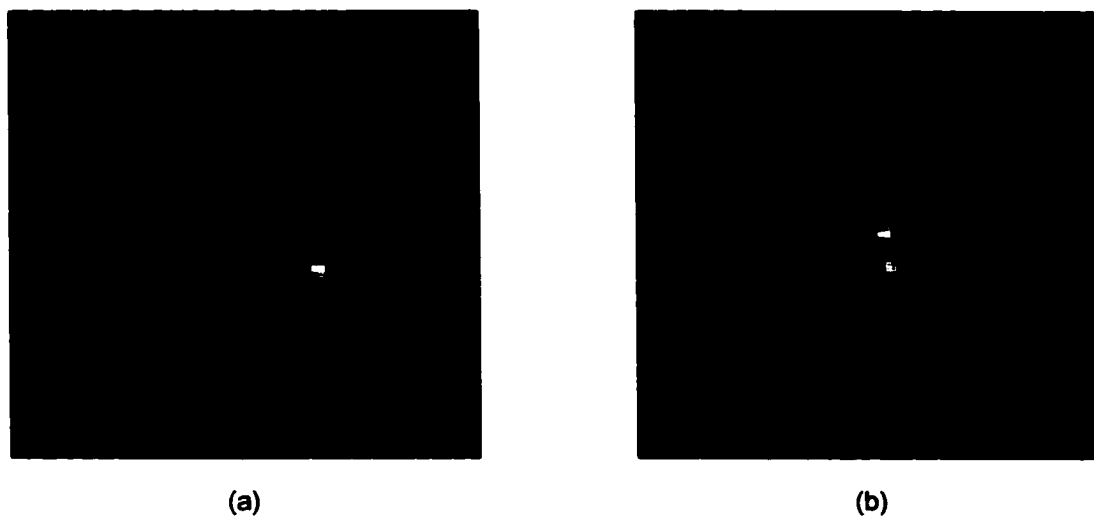


FIGURE 4.13. Two short-exposure images for a high level of turbulence,  $r_o = 0.05 m$ , and 8% additive Gaussian noise. (a) Image 1. (b) Image 2.



FIGURE 4.14. Binary stars. (a) Original object. (b) Reconstruction for high turbulence  $r_o = 0.05 m$ , 8% additive Gaussian noise case.

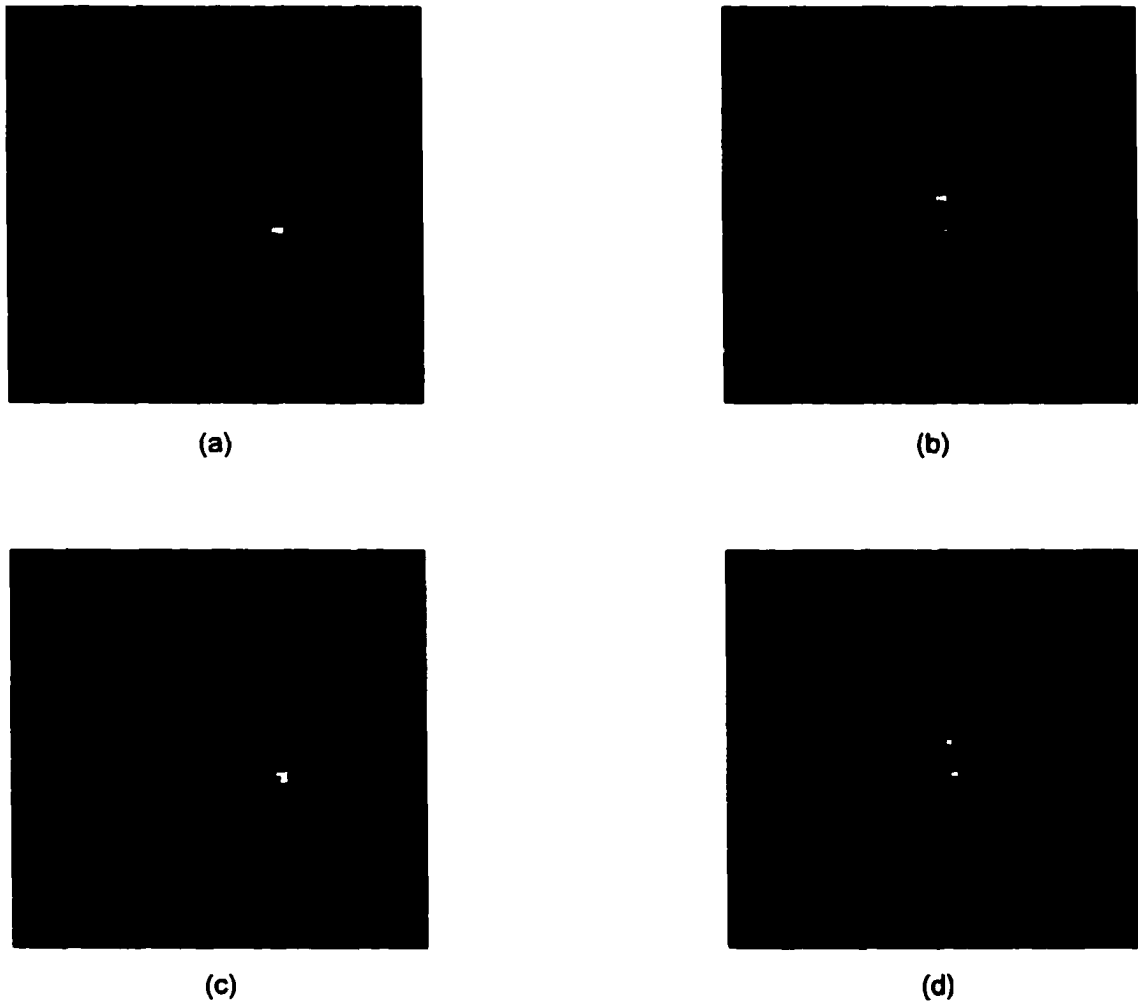


FIGURE 4.15. Two high turbulent degraded PSF's used for the 8% additive Gaussian noise case. (a) PSF 1. (b) PSF 2. (c) Reconstructed PSF 1. (d) Reconstructed PSF 2.



FIGURE 4.16. Two short-exposure images of binary stars, for a low level of turbulence,  $r_o = 0.2 m$ , and 10% of additive Gaussian noise. (a) Image 1. (b) Image 2.



FIGURE 4.17. Binary stars. (a) Original object. (b) Reconstruction for a low level of turbulence,  $r_o = 0.2 m$ , and 10% additive Gaussian noise case.

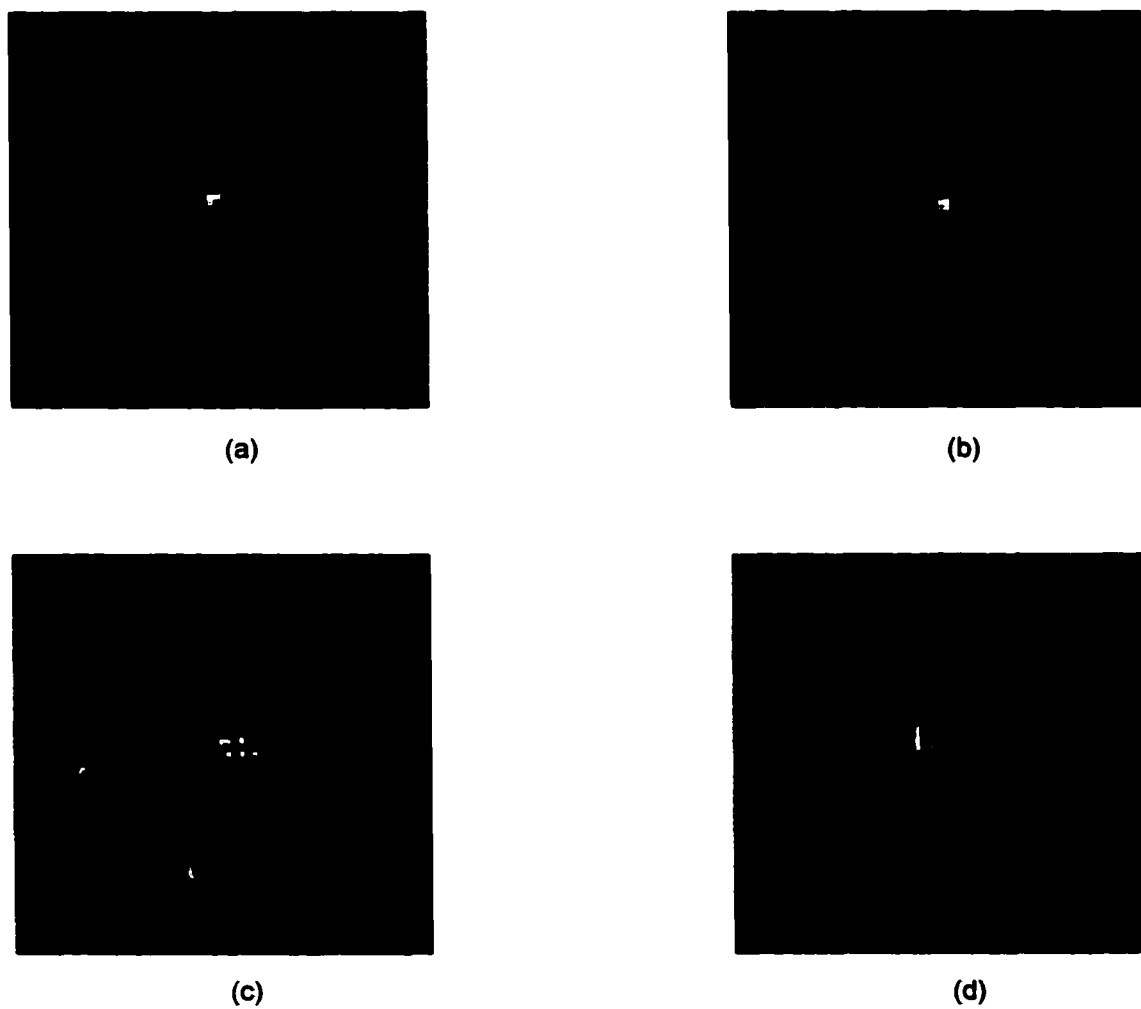


FIGURE 4.18. Low turbulent degraded PSF's, for the 10% additive Gaussian noise case. (a) PSF 1. (b) PSF 2. (c) Reconstructed PSF 1. (d) Reconstructed PSF 2.



FIGURE 4.19. Two moderate turbulent degraded ( $r_o = 0.1 m$ ) images of the cluster of stars. They are corrupted with 3% additive Gaussian noise. (a) Image 1. (b) Image 2.

#### 4.1.2 Cluster of Stars

The next example is a cluster of stars shown in Figure 4.20(a). Five different cases are presented, each with different levels of additive Gaussian noise. Two images of the cluster of stars that are moderately degraded by turbulence ( $r_o = 0.1 m$ ) are given in Figure 4.19. They are further corrupted with 3% additive Gaussian noise. For this example only the reconstructed objects for each case are shown. Figure 4.20(b) shows the reconstructed object for the 0% noise, low level of turbulence case. Once again the reconstruction for this noiseless case is excellent.

Figures 4.20(c), (d) and (e) show the reconstruction objects for the cases: 1% additive Gaussian noise and a low level of turbulence ( $r_o = 0.2 m$ ); 3% additive Gaussian noise and a moderate level of turbulence ( $r_o = 0.1 m$ ); 5% additive Gaussian noise and a low level of turbulence ( $r_o = 0.2 m$ ). Observe that up to 5% level of noise still permits good results.

The reconstructed object for the last case, 8% additive Gaussian noise and a

moderate level of turbulence ( $r_o = 0.1 m$ ), is given in Figure 4.20(f). Once again spurious background details make this a poor reconstruction, although the principal stars in the cluster still come through.

### 4.1.3 Galaxy

The final example, for computer simulated images, is a galaxy. See Figure 4.22(a). Two short-exposure picture of the galaxy are given in Figures 4.21(a) and (b). These are for a low level of turbulence,  $r_o = 0.2 m$ , and 5% additive Gaussian noise case.

For this example the level of turbulence is kept low,  $r_o = 0.2 m$ , while the level of noise is varied to form five different cases: 0%, 1%, 3%, 5% and 8% additive Gaussian noise. Reconstructed objects for these cases are shown in Figures 4.22(b), (c), (d), (e) and (f) respectively. They are good except the last one which shows a lot of spurious resolution.

## 4.2 Real Data

In this section the regularized image division method is tested through the usage of real data. Infrared images taken by John Garcia at Kitt Peak are used as inputs. They are images of hot sources against a cold background plate, taken with a OSC HgCdTe camera. The wavelength bandwidth was  $8 - 11 \mu m$ . The exposure time was  $\sim 0.02$  seconds, and the separation time between pictures was  $\sim 0.1$  seconds. All the targets were at 11.6 Km (slant path) range.

### 4.2.1 One Hot Source

The first example corresponds to a target composed of one hot source. A telescope with an F number equal to  $F/13$ , and a clear aperture of  $0.9 m$  was used. The imagery is coarsely pixelated. Two of the recorded images are shown in Figures 4.23(a) and 4.23(b). They were the inputs in the regularized image division algorithm.

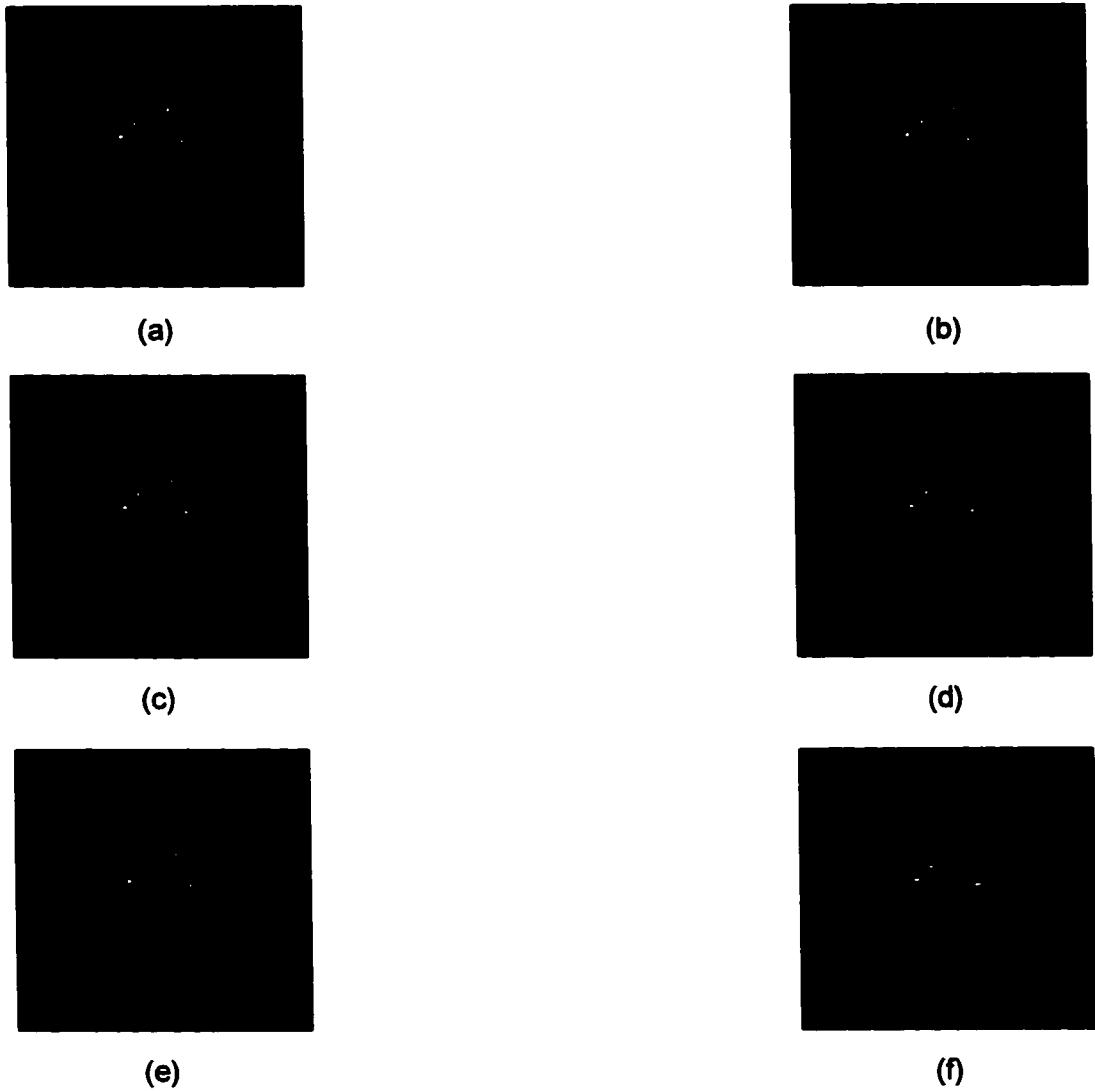


FIGURE 4.20. A cluster of stars. (a) Original object. (b) Reconstructed object for low level of turbulence, 0% additive Gaussian noise. (c) Reconstructed object for low level of turbulence,  $r_o = 0.2 m$ , 1% additive Gaussian noise. (d) Reconstructed object for moderate level of turbulence,  $r_o = 0.1 m$ , 3% additive Gaussian noise. (e) Reconstructed object for low level of turbulence,  $r_o = 0.2 m$ , 5% additive Gaussian noise. (f) Reconstructed object for moderate level of turbulence,  $r_o = 0.1 m$ , 8% additive Gaussian noise.



FIGURE 4.21. Two short-exposure pictures of a galaxy, for low turbulence  $r_o = 0.2$   $m$ , 5% additive Gaussian noise case. (a) Image 1. (b) Image 2.

The reconstructed object for this case is given in Figure 4.24. Compared to the original images, the reconstructed object looks much better in being more compact and regular in appearance.

#### 4.2.2 Two Hot Sources

The next case is a two hot source target. The sources are separated by 20  $cm$  ( $\sim 4$  pixels on the image plane). A F number equal to  $F/10$  was used. Two of the recorded images are shown in Figures 4.25(a) and 4.25(b).

The reconstructed object is shown in Figure 4.26. There it is possible to more cleanly resolve the two hot sources, although spurious background details appear in this reconstruction.

#### 4.2.3 Three Hot Sources

The final case is a target composed by three hot sources. The images were taken with a telescope with a F number equal to  $F/13$ , and a clear aperture of 0.9  $m$ . The two

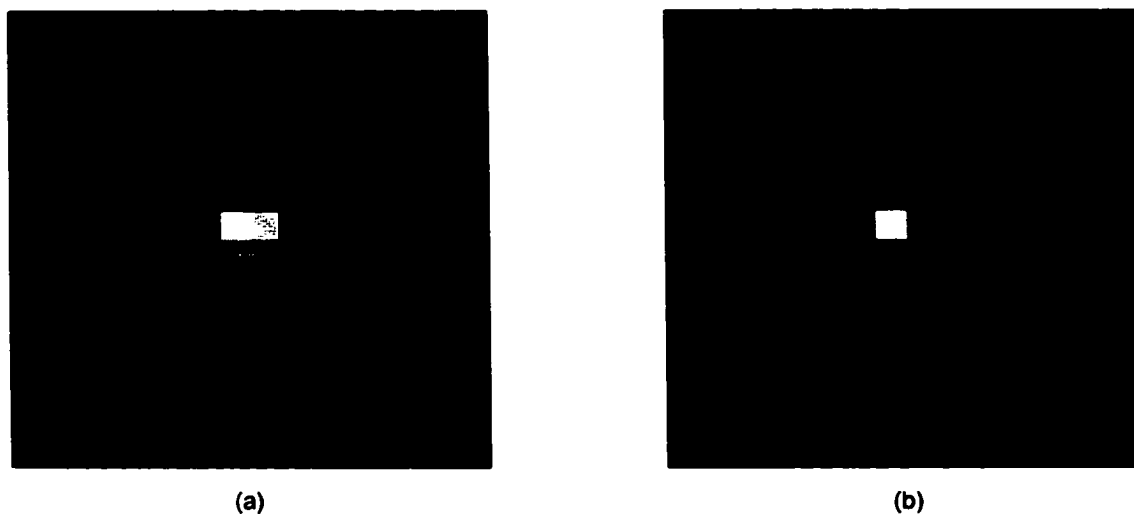


FIGURE 4.23. Two short-exposure images of a hot source. (a) Image 1. (b) Image 2.

images used as inputs in the algorithm are shown in Figures 4.27(a) and 4.27(b).

The reconstructed object for this target is shown in Figure 4.28. Notice that the three hot sources are better defined in the reconstruction than in the original images, although spurious background details appear.

### 4.3 Comparisons

In this section results from the regularized image division method are compared to results from three different methods: Ayers and Dainty's method [9], Lane's method [10] and Holmes' method [12]. The three of them use the same computer simulated example to test their algorithms. This example consists of an object, shown in Figure 4.29(a), and a PSF, shown in Figure 4.29(b). They are convolved to form images which are the inputs to these algorithms.

In order to use this example with the regularized image division algorithm a second PSF is required. Figure 4.30 shows a random PSF which is used as a second PSF during all the comparisons.

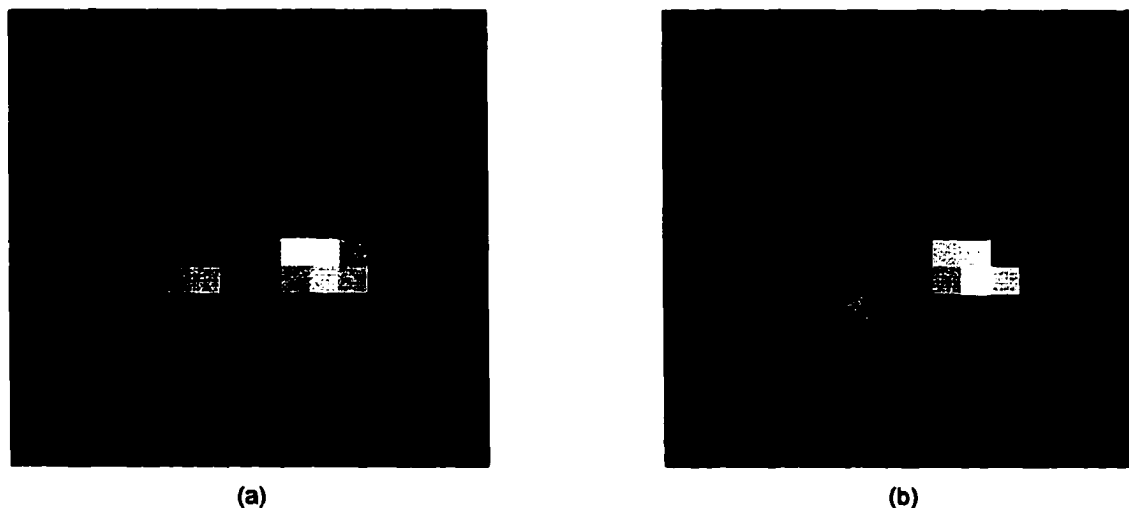


FIGURE 4.25. Two short-exposure images of a two hot source target. (a) Image 1. (b) Image 2.

### 4.3.1 Ayers and Dainty's Method

Ayers and Dainty created an iterative algorithm to attack the blind deconvolution problem [9]. It constrains the estimates of the object and PSF in the image and Fourier domains. Ayers and Dainty show in their paper [9] the results for a noiseless case. See Figures 4.31 and 4.32.

Results from the same noiseless example using the image division algorithm are presented in Figures 4.33(a) and 4.33(b). There it is possible to observe that the image division method produced better results since no spurious background details appear as in the outputs (Figures 4.31, 4.32) from Ayers and Dainty's method.

### 4.3.2 Lane's Method

Lane reformulated the blind deconvolution problem as an unconstrained minimization problem incorporating the image and Fourier constraints into an error metric [10]. He uses a conjugate gradient algorithm to solve the minimization problem. Results

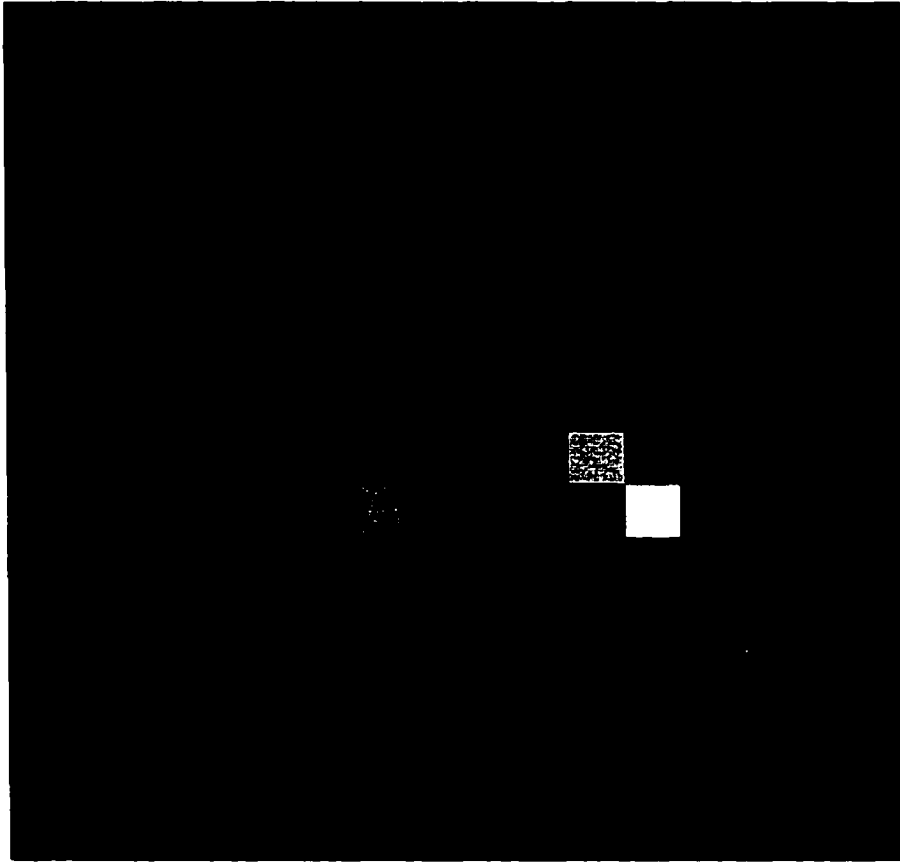


FIGURE 4.26. Reconstructed object for the two hot source target.

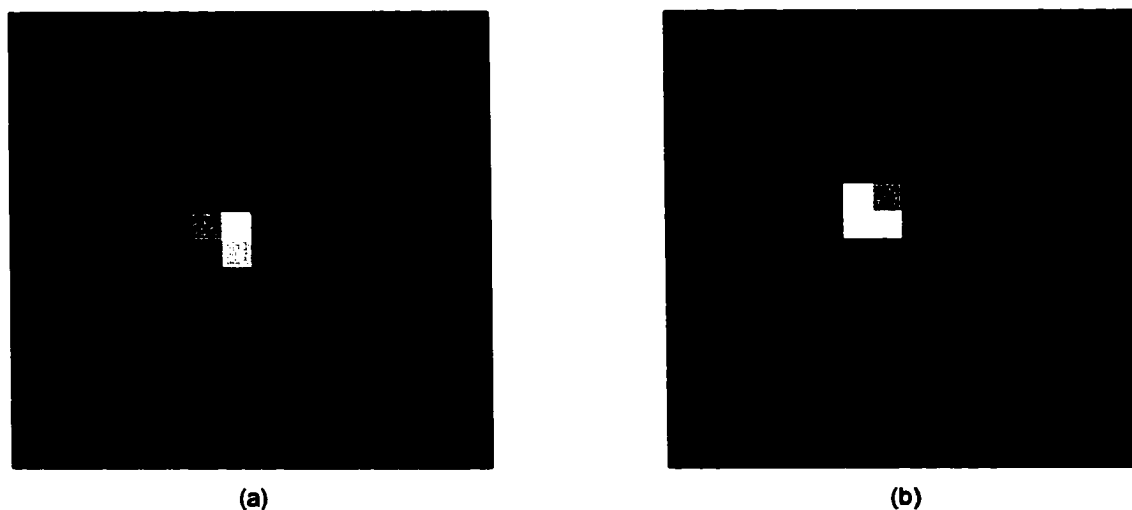


FIGURE 4.27. Two short-exposure images of a target composed by three hot sources.

from his method are shown in [10]. They are reproduced here in order to compare them to results yielded by the image division method. The noiseless case is shown in Figures 4.34 (a) and (b) (Lane shows only the worst solution obtained from five deconvolution trials). Lane also tested his method with Poisson corrupted images. These noisy cases are identified by the mean number of photons  $N$  at the brightest pixel in the convolution. Figures 4.35 (a) and (b) show the resulted object and resulted PSF respectively for  $N = 10^4$  photons, Figures 4.36 (a) and (b) the results for  $N = 10^3$  photons, and Figures 4.37 (a) and (b) the results for  $N = 10^2$  photons.

Results from the image division algorithm are shown as follows: Figures 4.33(a) and (b) for the noiseless case, Figures 4.38(a) and (b) for  $N = 10^4$  photons, Figures 4.39(a) and (b) for  $N = 10^3$  photons, and Figures 4.40(a) and (b) for  $N = 10^2$  photons. Notice that the results from the image division method are in general better than the results from Lane's method.

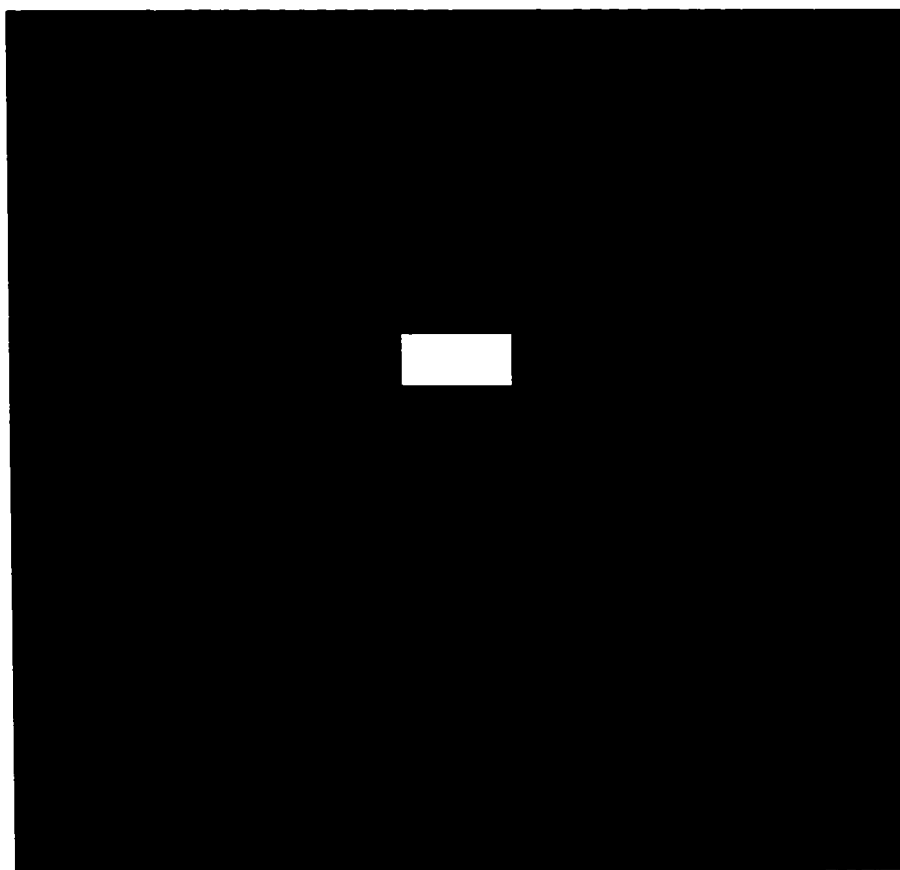


FIGURE 4.28. Reconstructed object for the three hot source object.



FIGURE 4.29. The object (a), and the PSF (b) used by Ayers and Dainty, Lane and Holmes.



FIGURE 4.30. Second PSF used on the regularized image division method.

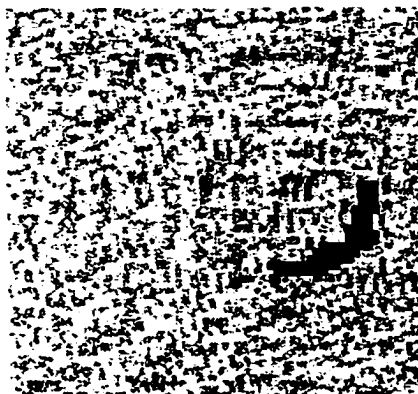


FIGURE 4.31. Reconstructed object for the noiseless case applying Ayers and Dainty's method.

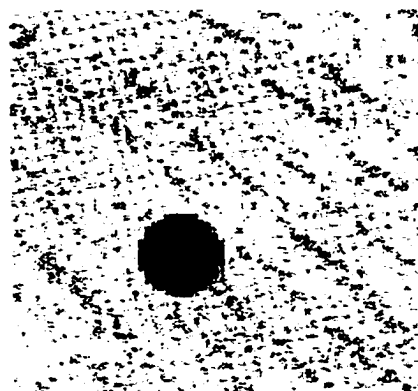


FIGURE 4.32. Reconstructed PSF for the noiseless case applying Ayers and Dainty's method.



FIGURE 4.35. Reconstructed object (a), and PSF (b), using Lane's method for an image corrupted with Poisson noise with  $10^4$  photons as a mean number of photons at the brightest pixel in the convolution

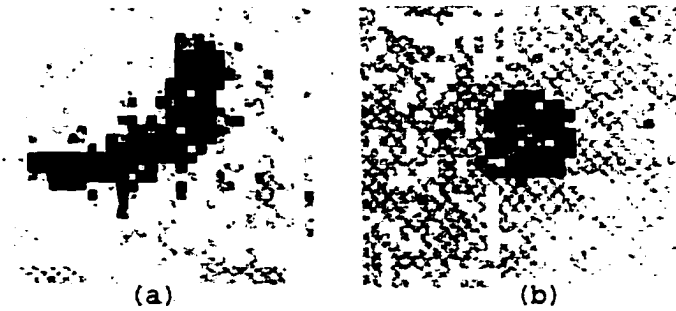


FIGURE 4.36. Reconstructed object (a), and PSF (b), using Lane's method for an image corrupted with Poisson noise with  $10^3$  photons as a mean number of photons at the brightest pixel in the convolution

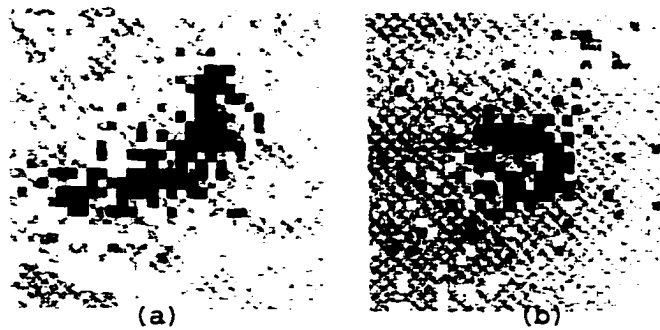


FIGURE 4.37. Reconstructed object (a), and PSF (b), using Lane's method for an image corrupted with Poisson noise with  $10^2$  photons as a mean number of photons at the brightest pixel in the convolution



FIGURE 4.38. Reconstructed object (a), and PSF 1 (b), using the image division algorithm for an image corrupted with Poisson noise with  $10^4$  photons as a mean number of photons at the brightest pixel in the convolution



FIGURE 4.39. Reconstructed object (a), and PSF 1 (b), using the image division algorithm for an image corrupted with Poisson noise with  $10^3$  photons as a mean number of photons at the brightest pixel in the convolution.



FIGURE 4.40. Reconstructed object (a), and PSF 1 (b), using the image division algorithm for an image corrupted with Poisson noise with  $10^2$  photons as a mean number of photons at the brightest pixel in the convolution

### 4.3.3 Holmes' Method

Holmes uses maximum-likelihood estimation (MLE) as a quantitative optimization criterion to solve the blind deconvolution problem. Results from his method are shown in Figure 4.41 for a Poisson noise corrupted image with 4000 photons per pixel, and Figure 4.42 for a Poisson noise corrupted image with 100 photons per pixel.

Results from the image division method are shown in Figure 4.43 for a Poisson noise corrupted images with 4000 photons per pixel and Figure 4.44 for a Poisson noise corrupted image with 100 photons per pixel. Comparing the image division results with Holmes' results shows that the image division method yields better results under similar conditions.



FIGURE 4.41. Result from Holmes' method for a Poisson noise corrupted image with 4000 photons per pixel.



FIGURE 4.42. Result from Holmes' method for a Poisson noise corrupted image with 100 photons per pixel.

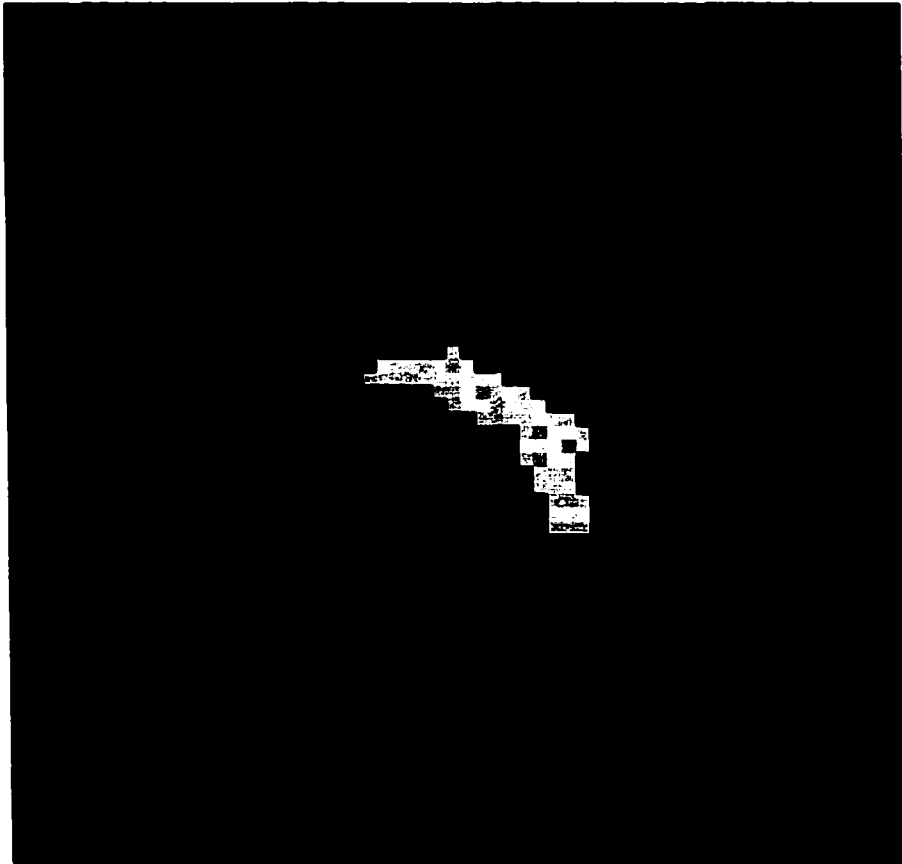


FIGURE 4.43. Result from the image division method for a Poisson noise corrupted images with 4000 photons per pixel.

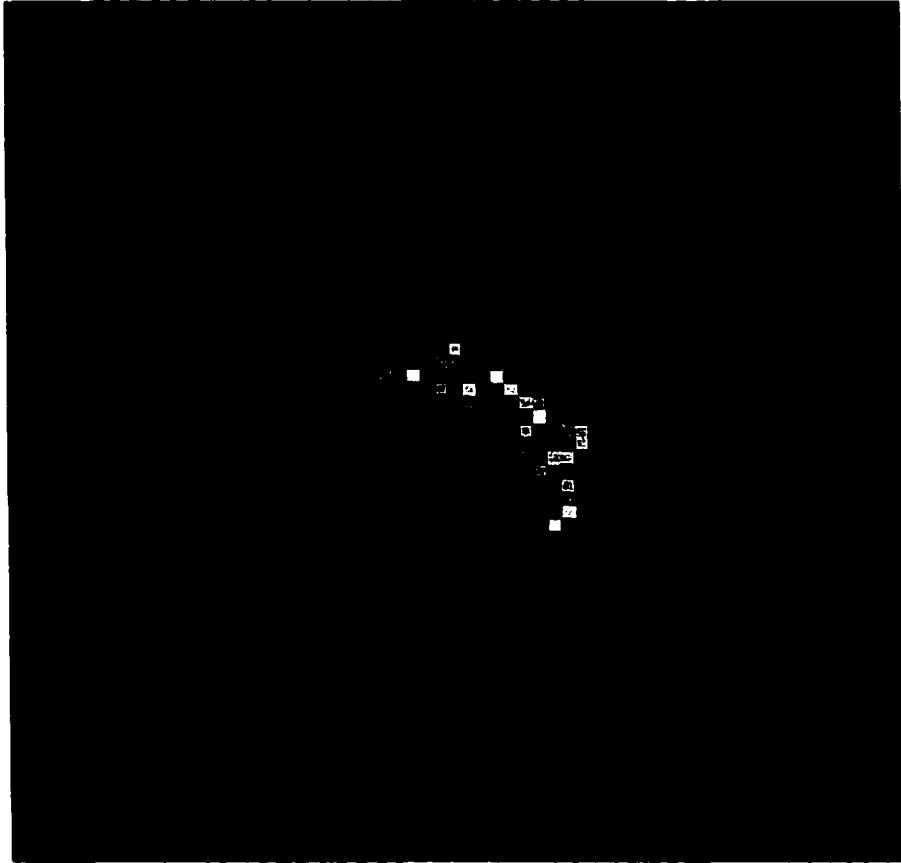


FIGURE 4.44. Result from the image division method for a Poisson noise corrupted images with 100 photons per pixel.

## Chapter 5

# CONCLUSIONS

### 5.1 Discussion

#### 5.1.1 Coping with PSF's with Different Supports

The regularization algorithm given in Chapter 3 implies that the two PSF's have the same support along the  $x_1$  direction, say  $K_{x_1}$ , and the same support along the  $x_2$  direction, say  $K_{x_2}$ . What if this is not the case? Apparently we should vary the four parameters  $K_{x_1}^{(1)}$ ,  $K_{x_2}^{(1)}$ ,  $K_{x_1}^{(2)}$ , and  $K_{x_2}^{(2)}$  in the algorithm loop (1)-(12) on subsection 3.2.5, for this general case. Varying four parameters instead of two parameters increases dramatically the number of searching trials (from  $2^k$  to  $2^{2k}$ , if each parameter takes  $k$  possible values), making the problem much more difficult to cope with (computationally speaking). However there is no need to vary the four parameters since when the estimated supports  $\hat{K}_{x_1}$  and  $\hat{K}_{x_2}$  equals the biggest of the supports of both PSF's, the correct solution is attained. The solution for the PSF with the smallest support shows zeros outside of its true support.

The following procedure also require the variation of two parameters. We can form two new images  $\tilde{i}^{(1)}$  and  $\tilde{i}^{(2)}$  through linear combinations of the old ones  $i^{(1)}$  and  $i^{(2)}$ :

$$\begin{aligned}\tilde{i}^{(1)} &\equiv a_1 i^{(1)} + a_2 i^{(2)}, \\ \tilde{i}^{(2)} &\equiv b_1 i^{(1)} + b_2 i^{(2)}, \quad a_1 + a_2 = 1, \quad b_1 + b_2 = 1, \quad a_1, a_2, b_1, b_2 > 0.\end{aligned}\tag{5.1}$$

Now from eq. (2.4) we can see that the new images are formed by net PSF's that obey, respectively,

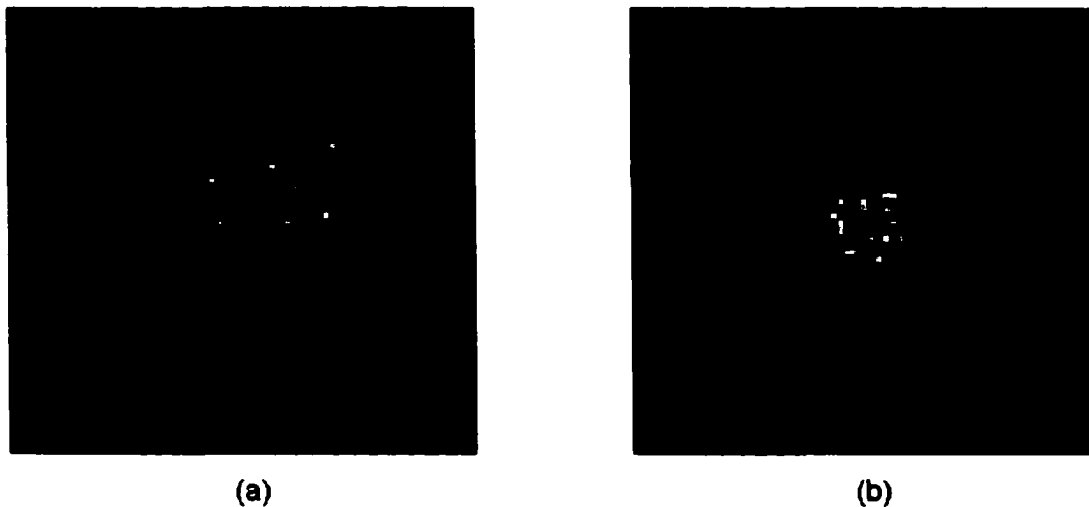


FIGURE 5.1. Two random PSF's with different supports. (a) PSF with a  $26 \times 26$  pixels support. (b) PSF with a  $10 \times 10$  pixels support.

$$\begin{aligned}\tilde{s}^{(1)} &\equiv a_1 s^{(1)} + a_2 s^{(2)}, \\ \tilde{s}^{(2)} &\equiv b_1 s^{(1)} + b_2 s^{(2)}.\end{aligned}\tag{5.2}$$

This new PSF's  $\tilde{s}^{(1)}$ , and  $\tilde{s}^{(2)}$  have the same  $x_1$  support and the same  $x_2$  support, since each of them is a weighted sum of both old PSF's.

Figure 5.1 shows two random PSF's with different support (a)  $26 \times 26$  pixels, (b)  $10 \times 10$  pixels. These PSF's are convolved with the object shown in Figure 4.29 (a), and 8% Gaussian noise is added to form two images, see Figure 5.2. These images are used as inputs in the image division algorithm. Figure 5.3 shows the reconstructed PSF's. Now the two original images are combined following the procedure given above, and these new combined images are used as input in the image division algorithm. Figure 5.4 shows the reconstructed PSF's for the last case. The reconstructed object for both cases are given in Figure 5.5. We can observe that they are very similar, which confirms that both procedures yield similar results.

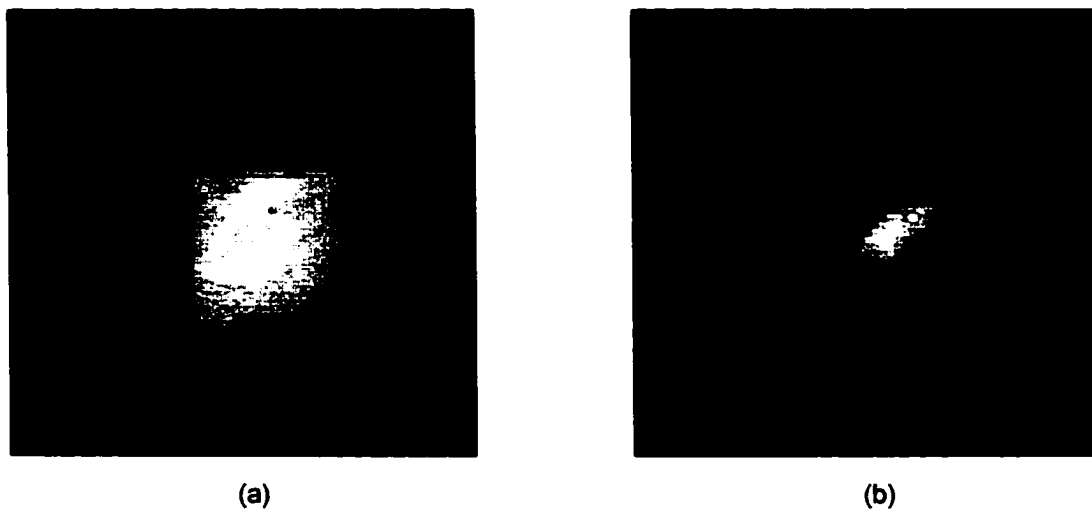


FIGURE 5.2. Two images formed with PSF's with different supports. (a) Image with a PSF  $26 \times 26$  pixels. (b) Image with a PSF  $10 \times 10$  pixels.

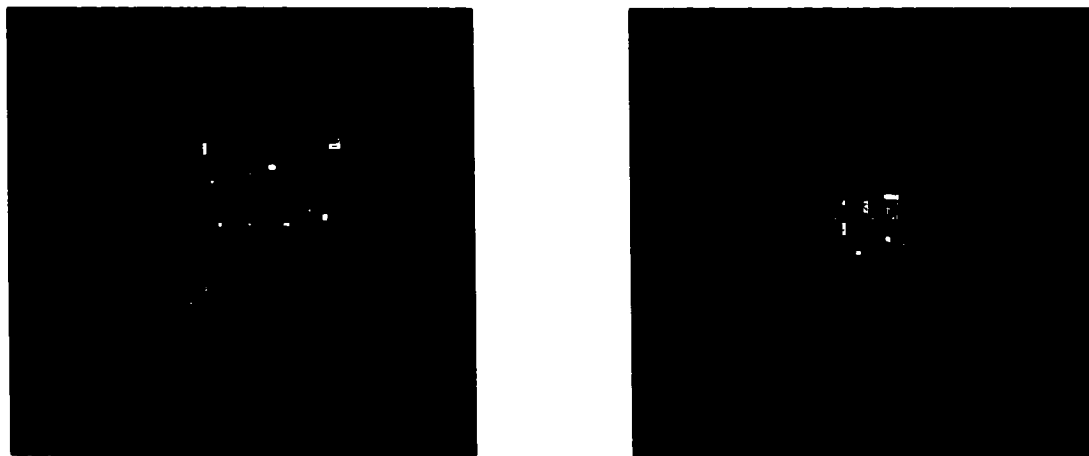


FIGURE 5.3. Reconstructed PSF's using the original images.



FIGURE 5.4. Reconstructed PSF's using the combined images.



FIGURE 5.5. Reconstructed objects. (a) Using the original images. (b) Using the combined images.

### 5.1.2 Minimum of Data Inconsistency $e$

The regularized image division approach assumes that the best reconstructed result is obtained when data inconsistency  $e$  has a grand minimum [see step(12)]. In order to verify this assumption Figure 5.6 shows the plot of  $e$  versus  $\hat{K}_1$  and  $\hat{K}_2$  for the 5% additive Gaussian noise case of Sec. 4.1.1 d). From there it is possible to show that  $e$  has a grand minimum at  $\hat{K}_1 = 27$  and  $\hat{K}_2 = 26$  pixels. The reconstructed object yielded by this support is shown in Figure 4.11, and it is indeed the best reconstructed result.

Notice however, that there are other points in Figure 5.6 which are nearly as low as the grand minimum. Now, considering that each point in this figure has an associated bar error, then the grand minimum is not clearly defined. In order to deal with this problem we proceed to find a polynomial of degree four to fit the data in a least-squares sense. Figure 5.7 shows a plot of the fitting polynomials. We can observe that the grand minimum is still the point at  $\hat{K}_1 = 27$  and  $\hat{K}_2 = 26$  pixels. Now the point at  $\hat{K}_1 = 27$  and  $\hat{K}_2 = 28$  pixels is too close to the grand minimum that it is interesting to take a look to the solution given by this support. From Figure 5.8 we can observe that this result is almost as good as the result from the grand minimum. Therefore the method proposed by the regularized image division algorithm, for finding the "best result", is a robust one.

### 5.1.3 Residual Errors in the System of Equations

Working with noisy data produces residual errors in the right-hand sides of eqs. (3.19) and (3.20), since the quotient of the spectra of the images  $D_n = I_n^{(1)}/I_n^{(2)}$  is not longer equal to the quotient of the spectra of the PSF's  $\tau_n^{(1)}/\tau_n^{(2)}$ . How large are these errors? Let us find out. By using eq. (2.7) on both images we get

$$e_n = \tau_n^{(1)} - D_n \tau_n^{(2)} = D_n N_n^{(2)} / O_n - N_n^{(1)}, \quad n = 0, 1, \dots, N^2 - 1 \quad (5.3)$$

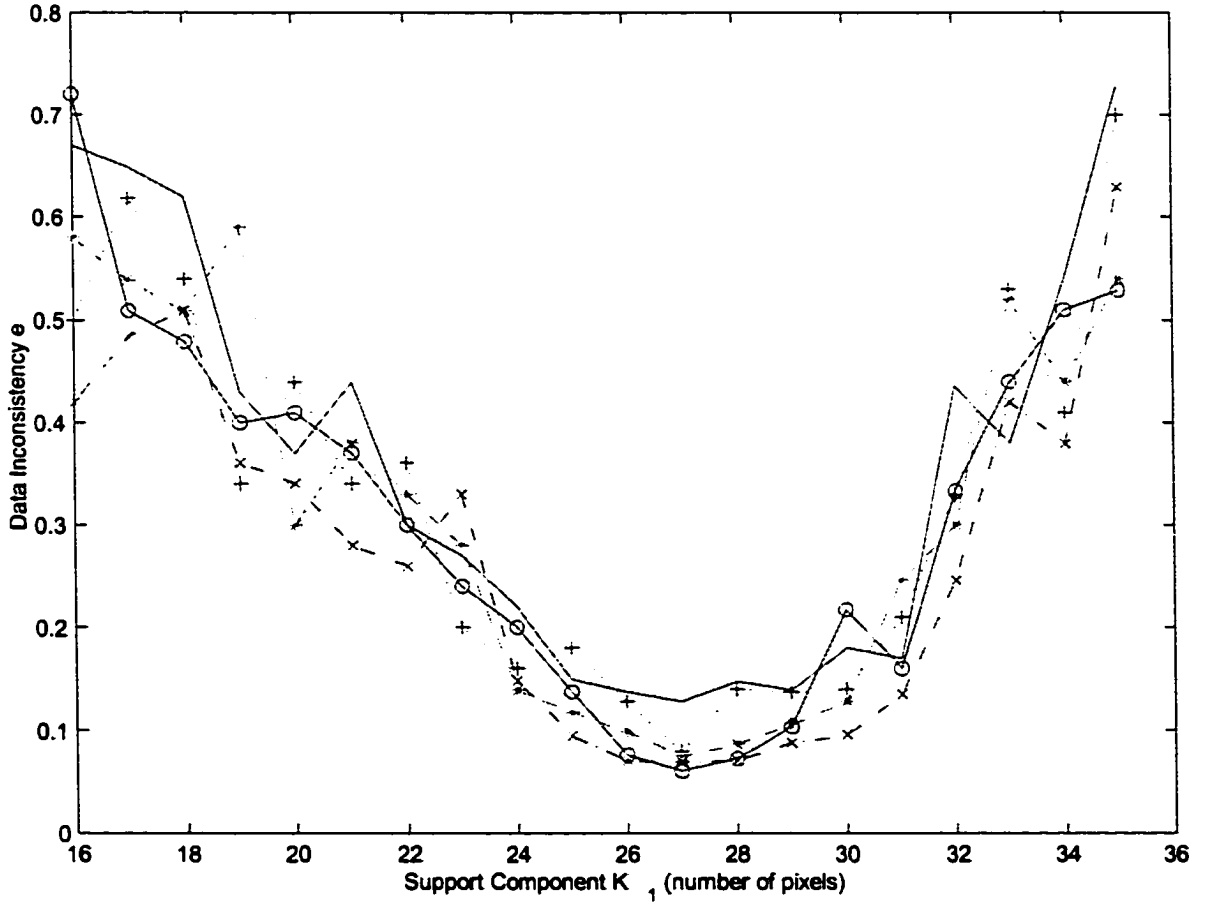


FIGURE 5.6. Plot of data inconsistency  $e$  versus support component  $\hat{K}_1$  for various values of component  $\hat{K}_2$ :  $\hat{K}_2 = \hat{K}_1 - 2$  (pluses, +),  $\hat{K}_2 = \hat{K}_1 - 1$  (open circles, o),  $\hat{K}_2 = \hat{K}_1$  (asterisks, \*),  $\hat{K}_2 = \hat{K}_1 + 1$  (crosses, x),  $\hat{K}_2 = \hat{K}_1 + 2$  (continuous line).

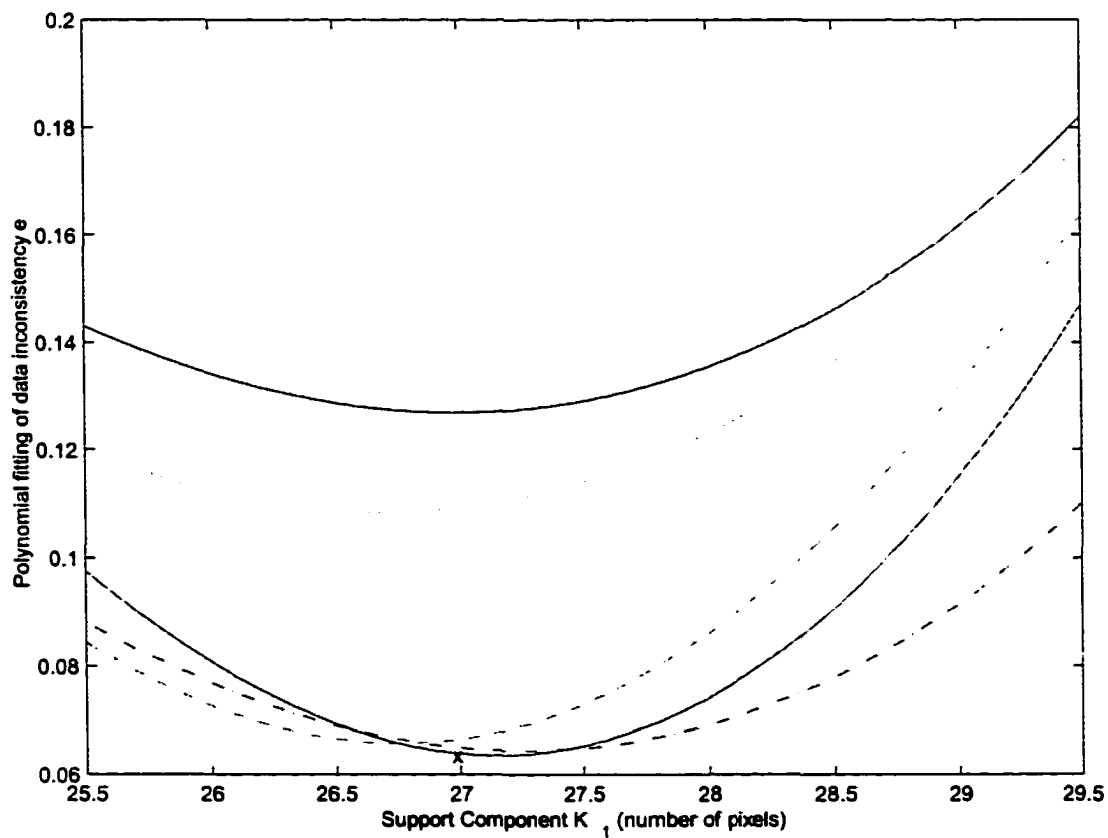


FIGURE 5.7. Plot of polynomial fitting of data inconsistency  $e$  versus support component  $\hat{K}_1$  for various values of component  $\hat{K}_2$ :  $\hat{K}_2 = \hat{K}_1 - 2$  (dot line),  $\hat{K}_2 = \hat{K}_1 - 1$  (continuous line),  $\hat{K}_2 = \hat{K}_1$  (dashed line),  $\hat{K}_2 = \hat{K}_1 + 1$  (dashed-dot line),  $\hat{K}_2 = \hat{K}_1 + 2$  (continuous line). The cross points to the grand minimum at  $\hat{K}_1 = 27$  and  $\hat{K}_2 = 26$  pixels.

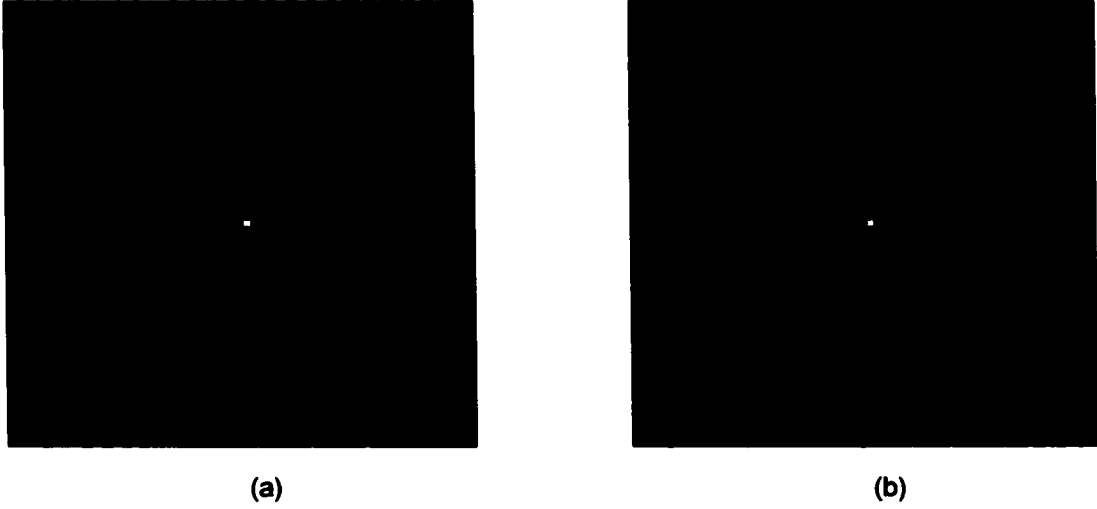


FIGURE 5.8. Reconstructions for the binary star system, low level of turbulence, 5% additive Gaussian noise case. (a) Reconstructed object for a support of  $\hat{K}_1 = 27$  and  $\hat{K}_2 = 26$  pixels. (b) Reconstructed object for a support of  $\hat{K}_1 = 27$  and  $\hat{K}_2 = 28$  pixels.

Compare eqs. (5.3) with the noiseless equivalent eqs. (3.14). Since the latter are homogeneous equations, this leaves the right-hand sides of eqs. (5.3) as the residual errors of eqs. (3.19) and (3.20) for noisy data. Taking account these residual errors eq. (3.21) becomes

$$H\vec{x} = \vec{b} + \vec{e}, \quad (5.4)$$

where  $\vec{e}$  is a  $N^2 \times 1$  vector whose components are the residual errors  $e_n$ .

We can see that these residual errors depend on the computed data values  $D_n$  and on the spectra of the object  $O_n$  and the additive noise in both images  $N_n^{(1)}$  and  $N_n^{(2)}$ , which of course are unknowns. However using a computer simulated example we can observe how these residual errors behave as the noise level increases. Running the same one-dimensional case from Sec. 3.2.1, but now generating a pair of images for three different levels of noise (1%, 5%, and 10%), we can compute the residual errors  $e_n$  from the three noise-level cases. The latter are plotted, along with the right-hand

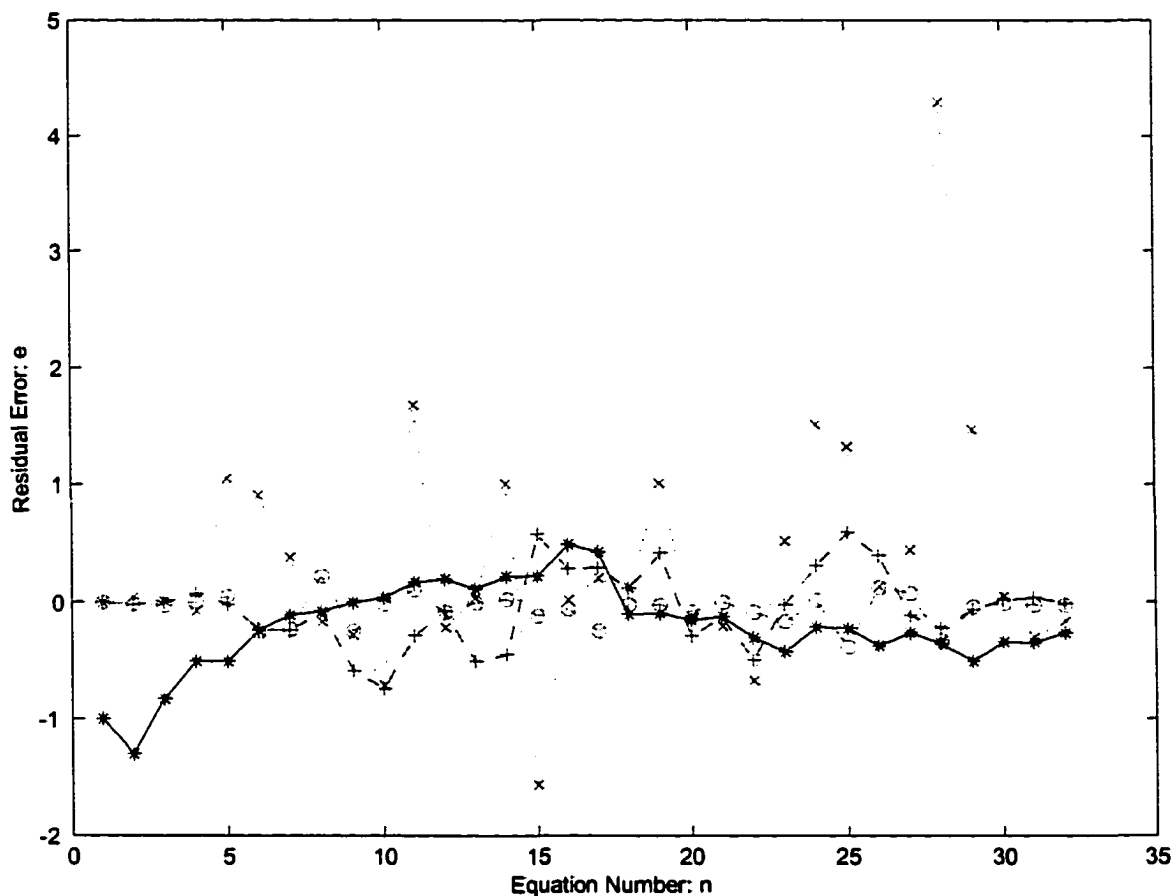


FIGURE 5.9. The residual error for eqs. (3.19) and (3.20) for different levels of noise. (a) 1% (open circles), (b) 5% (pluses), (c) 10% (crosses), (d) Right-hand sides of eqs. (3.19) and (3.20) (asterisks)

sides of eqs. (3.19) and (3.20) (the components of vector  $\vec{b}$  in eq. (3.21)), on Figure 5.9.

From Figure 5.9 we observe that while the residual errors for the 1% noise level (open circles) stay close to the abscissa axis, the residual errors for the 10% noise level (crosses) oscillate with amplitudes that much exceed the average values of the right-hand sides of eqs. (3.19) and (3.20). This partially explains why the results of the algorithm for this level of noise are generally not good.

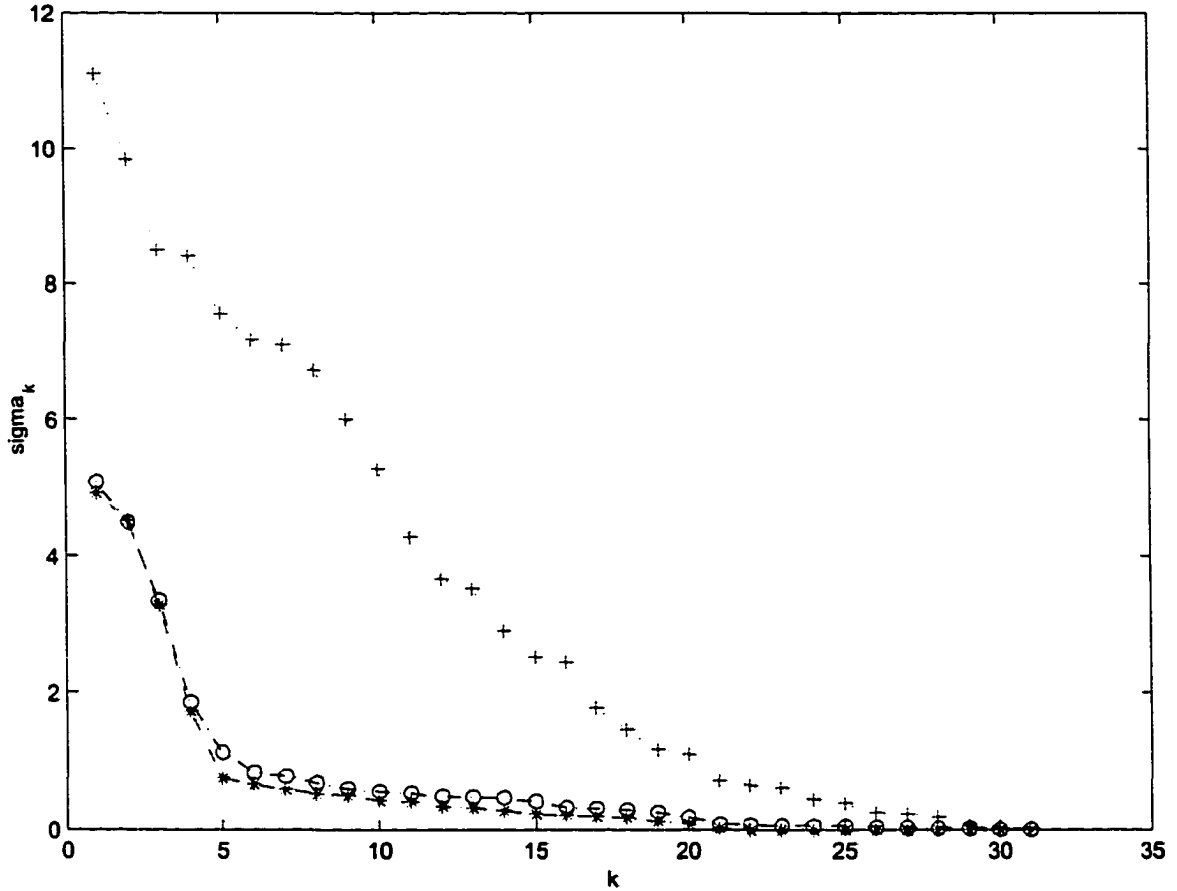


FIGURE 5.10. Singular values of matrix  $H$  from eq. (3.21), for three levels of noise: (a) 0% (asterisks), (b) 5% (open circles), and (c) 10% (pluses).

#### 5.1.4 Singular Value Decomposition

In Chapter 2 the singular value decomposition was shown to be a tool for analyzing ill-conditioned system of equations. Using the example from Sec. 3.2.1, we compute the singular values for the matrix  $H$  in eq. (3.21) for the noise levels 0%, 5%, and 10%. The results are plotted in Figure 5.10.

As it is observed in this figure the singular values for the noiseless case decay to zero faster than the singular values for the noisy data. This is typical behavior for an ill-conditioned matrix. The singular values for the 10% noise-level case decay the least

fast of the three cases. Would this mean that the matrix  $H$  is "less ill-conditioned" as the level of noise increases? Yes indeed, as it can be confirmed by computing the condition number of  $H$  for the three cases. For the noiseless case the condition number of  $H$  is the astronomical number of  $4.4 \times 10^{17}$  (confirming that for this case  $H$  is rank deficient), for the 5% noise-level case it is  $8.1 \times 10^2$ , and for the 10% noise-level it is  $2.1 \times 10^2$ . This can be explained (as in Sec. 3.2.1) by the fact that the noise makes the matrix  $H$  full rank by breaking the ambiguity in the solution of eqs. (3.19) and (3.20).

However although the matrix  $H$  becomes "less ill-conditioned" (or, more regularized) as the level of noise increases, the elements of  $H$  become less accurate as this happens. In eq. (5.4) the residual-error vector  $\vec{e}$  was written on the right-hand side, but the truth is that the errors due to the noise are inside the matrix  $H$ , since it is in the computation of  $H$  that the noisy data  $D_n$  are used, see eqs. (3.19) and (3.20). Therefore it is more transparent to rephrase the problem as

$$H\vec{x} = (H_o + \Delta)\vec{x} = \vec{b}, \quad (5.5)$$

where  $H_o$  is the  $H$  matrix for the noiseless case and  $\Delta$  is a perturbation matrix (the difference between the noisy matrix  $H$  and the noiseless matrix  $H_o$ ). To get an idea of the "size" of this perturbation for different levels of noise, let us compute the quotient of the  $L^2$ -norm of the perturbation matrix  $\Delta$  over the  $L^2$ -norm of the noiseless matrix  $H_o$ , for the 5%, and 10% noise-level cases. This would give us some measurement of the relative error present in the noisy matrix  $H$  [31]

$$e_r = \frac{\|\Delta\|_2}{\|H_o\|_2}. \quad (5.6)$$

Now, for the 5% noise-level case  $e_r = 0.15$ , while for the 10% noise-level case  $e_r = 1.75$ . Doubling the level of noise makes the perturbation ten times bigger!

### 5.1.5 A Filter for the System of Equations

The relative error of the noisy data  $D_n = I_n^{(1)}/I_n^{(2)}$  can be computed using the following expression:

$$\delta_n = \frac{\text{abs}(D_n - D_{on})}{\text{abs}(D_{on})}, \quad (5.7)$$

where  $D_{on}$  is the quotient of the PSF's  $\tau_n^{(1)}/\tau_n^{(2)}$ . Using the example from Sec. 3.2.1 for a 5% level of noise case,  $\delta_n$  can be computed with eq. (5.7). Figure 5.11 plots  $\delta_n$  along with the absolute value of the image spectrum  $I_n^{(2)}$  versus frequency.

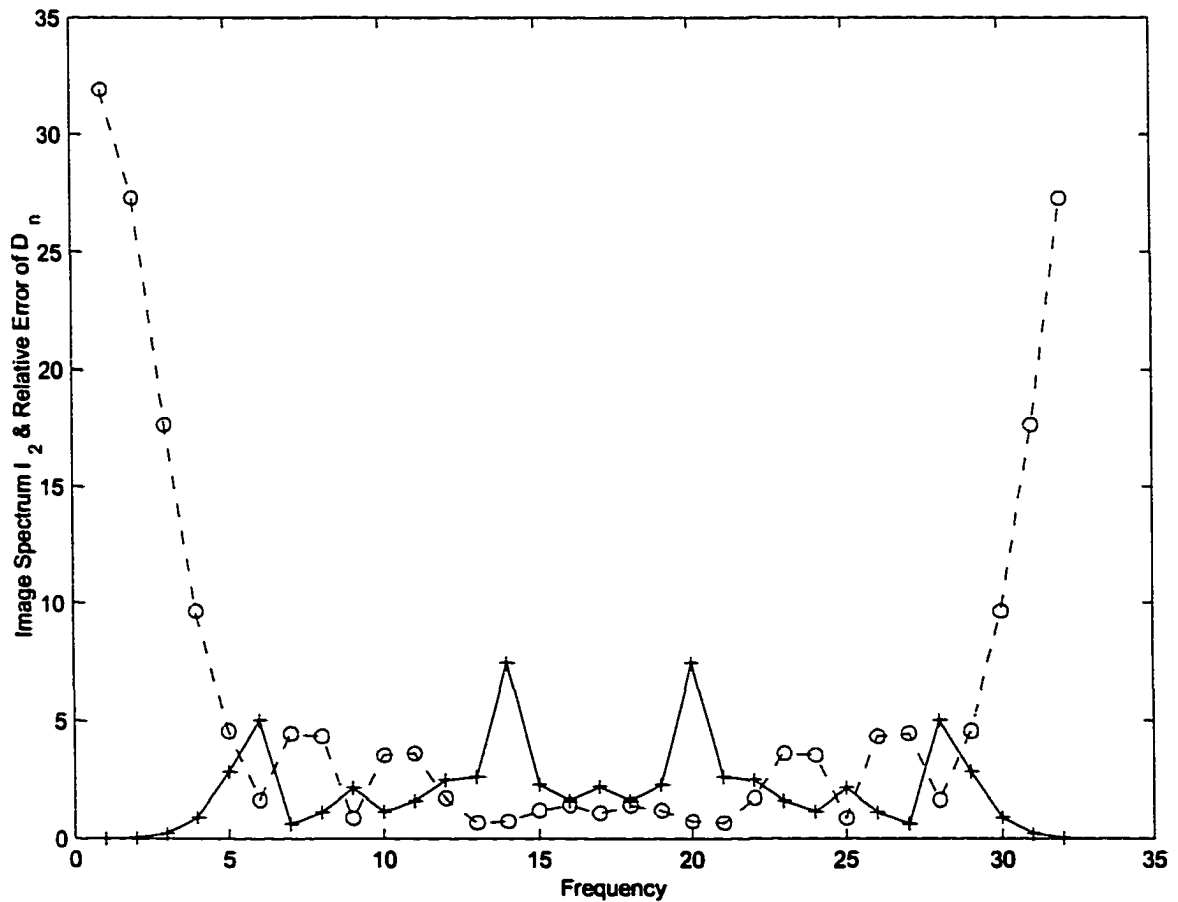


FIGURE 5.11. Graphic of the relative error on  $D_n$ :  $\delta_n$  (pluses), and the absolute value of the image spectrum  $I_n^{(2)}$  (open circles) versus frequency.

degraded images with additive Gaussian noise up to 5%. It also produces good results when infrared short-exposure images are used. Comparisons with results from other methods used to solve the blind deconvolution problem (Ayers and Dainty's method, Lane's method and Holmes' method) show that the image division method yields similar or better results than these under similar conditions (using the same object, PSF, and level of Poisson noise). We have tested the image division method with two different kind of noise: Gaussian additive, which is independent of the image, and Poisson which depends on the image data. In both cases we achieved good results as long as the level of noise is kept low enough: 5% for additive Gaussian noise, and  $N = 100$  photons as the average number of photons per pixel for Poisson noise.

The advantages of the approach are:

1. The fidelity of its outputs.
2. Its linearity and hence potential speed.
3. That it is of fixed length and avoids an open-ended search of solution space.
4. That it needs but two short-exposure images as inputs.
5. That it allows the incorporation of prior knowledge of the object and PSF's.
6. That it yields good results when tested with images corrupted with two different kinds of noise: additive Gaussian noise and Poisson noise.

It is clear that prior knowledge of the object and PSF's is a key element in the implementation of the image division algorithm. The support search can be narrowed through the use of any prior knowledge of PSF support. The method by which positivity is enforced can also be improved. Replacing the negative values by zeros (steps (4) and (7) of the algorithm) does not permit data consistency. Recourse to a nonlinear approach such as maximum entropy permits data consistency [15], [14]. A nonlinear approach can also be used to get the object estimate once the PSF estimate has been found, instead of using plain inverse filtering. This could make the image division algorithm a more robust method, capable of dealing with the higher levels of noise that are commonly encountered in real data.

## REFERENCES

- [1] J.C. Dainty (ed): *Laser Speckle and Related Phenomena*, 2nd. ed., Topics Applied Physics Vol. 9 (Springer, Berlin, Heidelberg, New York 1982).
- [2] A. Labeyrie: "Attainment of diffraction-limited resolution in large telescopes by Fourier analyzing speckle patterns in star images," *Astron. Astrophys.* 6, 85-87 (1970).
- [3] A. W. Lohmann, G. Weigell, and B. Wirmtzer: "Speckle masking in astronomy: triple correlation theory and applications," *Appl. Opt.* 22, 4028-4037 (1983).
- [4] H. Bartelt, A. W. Lohmann, and B. Wirmtzer: "Phase and amplitude recovery from bispectra," *Appl. Op.* 23, 3121-3129 (1984).
- [5] J. Primot, G. Rousset, and J. Fontanella: "Deconvolution from wavefront sensing: a new technique for compensating turbulence degraded images," *J. Opt. Soc. Am.* 7, 1598-1608 (1990).
- [6] J. D. Gonglewski, D. G. Voelz, J. S. Fender, D. C. Dayton, B. K. Spielbusch, and R. E. Pierson: "First astronomical application of postdetection turbulence compensation: images of  $\alpha$  Aurige,  $\nu$  Ursae Majoris, and  $\alpha$  Germinorum using self-referenced speckle holography," *Appl. Opt.* 29, 4527-4529 (1990).
- [7] J. H. Hardy: "Active Optics: a new technology for the control of light," *Proc. IEEE* 66, 651-697 (1978).
- [8] C. S. Gardner, B. M. Welsh, and L. A. Thompson: "Design and performance analysis of adaptive optical telescopes using laser guide stars," *Proc. IEEE* 78, 1721-1743 (1990).
- [9] G. Ayers, J. C. Dainty: "Iterative blind deconvolution method and its applications," *Opt. Letter* 13, 547 (1988).
- [10] R. G. Lane: "Blid deconvolution of speckle images," *J. Opt. Soc. Am.*, A9, 1508 (1992).
- [11] B. R. Frieden: "An exact, linear solution to the problem of imaging through turbulence," *Opt. Commun.* 150, 15-21 (1998).
- [12] T. J. Holmes: "Blind deconvolution of quantum-limited incoherent imagery: maximum-likelihood approach", *J. Opt. Soc. Am.*, A9, No. 7, 1052-1061 (1992).
- [13] J. W. Goodman: *Introduction to Fourier Optics*, McGraw-Hill.

## REFERENCES –continued

- [14] P. A. Jansson: Deconvolution of Images and Spectra, 2nd. ed.(Academic, San Diego, Calif., 1997).
- [15] B. R. Frieden: "Image enhancement and restoration," in Picture Processing and Digital Filtering, T. S. Huang, ed. Vol. 6 of Topics in Appl. Physics (Springer-Verlag, New York, 1975), p. 221
- [16] A. K. Katsaggelos (Ed.): Digital Image Restoration, Vol. 23 of Springer Series in Information Sciences (Springer-Verlag Berlin Heidelberg 1991).
- [17] M. Z. Nashed: IEEE Trans. AP-29, 220-231 (1981).
- [18] P. C. Hansen: Rank-Deficient and Discrete Ill-Posed Problems, Siam (1998).
- [19] C. L. Lawson, R. J. Hanson: Solving Least squares Problems, (Prentice-Hall, Inc., Englewood Cliffs, NJ 1974).
- [20] G. Dahlquist, A. Björck: Numerical Methods, (Prentice-Hall, Inc., Englewood Cliffs, NJ 1974).
- [21] C. Siva Ram M., K. N. Balasubramanya M., S. Aluru: New Parallel Algorithms for Direct Solution of Linear Equations (John Wiley & Sons 2001).
- [22] E. J. Kontoghiorghes: Parallel Algorithms for Linear Models, (Kluwer Academic Publishers 2000).
- [23] A. A. Shabana: Computational Dynamics, (John Wiley & Sons, Inc. 2001).
- [24] A. Björck: "A General Updating Algorithm for Constrained Linear Least Squares Problems", SIAM J. Sci. Stat. Comput., Vol 5, No. 2, 394-402, (June 1984).
- [25] M. Wei: Supremum and Stability of Weighted Pseudoinverses and Weighted Least Squares Problems, (Nova Science Publishers, Inc., Huntington, N. Y., 2001).
- [26] R. W. Farebrother: Linear Least Squares Computations, (Marcel Dekker, Inc., N. Y. and Basel, 1988).
- [27] J. W. Goodman: Statistical Optics, (John Wiley & Sons 1985).
- [28] B. R. Frieden: "Probability, Statistical Optics and Data Testing", 2nd ed. (Springer-Verlag, New York, 1991).

## REFERENCES -continued

- [29] S. Shaklan: "Multiple Beam Correlation Using Single-mode Fiber Optics with Applications to Interferometric Imaging," OSC Dissertation, U. of A. (1989).
- [30] A. Biran, M. Breiner: "Matlab for Engineers," (Addison-Wesley 1996).
- [31] The Student Edition of MATLAB, (Prentice-Hall, Englewood Cliffs, NJ 1995).
- [32] S. L. Campbell, C. D. Meyer, Jr.: Generalized Inverses of Linear Transformations, (Pitman 1979).
- [33] M. Z. Nashed, editor: Generalized Inverses and Applications, (Academic Press, N. Y., San Francisco, London 1976).
- [34] A. N. Tikhonov, V. Y. Arsenin: Solutions of Ill-Posed Problems, (John Wiley & Sons 1977).
- [35] B. de Moor, P. V. Dooren: "Generalization of the Singular Value and QR Decompositions", SIAM J. Matrix Anal. Appl., Vol. 13, No. 4, 993-1014, (Oct. 1992).
- [36] K. T. Knox and B. J. Thompson: "Recovery of images from atmospherically degraded short-exposure photographs," Astroph. J. Lett. 193, L45-L48 (1974).
- [37] Mathcad User's Guide, (MathSoft Inc. 1995).